UNIVERSITÀ DEGLI STUDI FIRENZE

DOTTORATO DI RICERCA IN ENERGETICA E TECNOLOGIE INDUSTRIALI E AMBIENTALI INNOVATIVE

CICLO XXXIII
COORDINATORE Prof. Giampaolo Manfrida

Development of an Integrated Procedure for Aerodynamic and Aeromechanic Design of Gas Turbine Engines

Settore scientifico disciplinare ING-IND/08

PhD Candidate	**Tutor**
Eng. Sara Biagiotti	**Prof. Andrea Arnone**
_____	_____

Co-ordinatore
Prof. Giampaolo Manfrida

_____

Firenze 2017/2020

Development of an Integrated Procedure for Aerodynamic and Aeromechanic Design of Gas Turbine Engines

Settore scientifico disciplinare ING-IND/08

PhD Candidate	**Tutor**
Eng. Sara Biagiotti	**Prof. Andrea Arnone**
Department of Industrial Engineering, Univerity of Florence	*Department of Industrial Engineering, Univerity of Florence*

Co-Tutor

Prof. Michele Marconcini	**Dr. Eng. Alberto Scotti Del Greco**
Department of Industrial Engineering, Univerity of Florence	*Baker Hughes, Italy*

Firenze 2017/2020

"Rare sono le persone che usano la mente, poche coloro che usano il cuore e uniche coloro che usano entrambi."

Rita Levi Montalcini

Abstract

The design loop of turbomachinery blade rows consists of different phases, ranging from the aerodynamic, the dynamic, to the aeromechanic one. Current trends move towards an integrated design, which strive to combine all these disciplines together. The aim is to maximize the aerodynamic performance and, at the same time, to avoid the vibration issues due to forced response and flutter phenomena.

The focus of this thesis is the development of an integrated procedure for the aerodynamic and aeromechanic design of axial gas turbine blades, based on numerical CFD simulations.

The procedure starts from the aerodynamic design phase devoted to evaluating the performance of the whole turbine domain. Steady and unsteady analyses allow the detailed analysis of the flow field and the derivation of the main physical quantities. These analyses have been carried out on a heavy-duty low pressure turbine module designed by Baker Hughes, selected as test case. A comparison between numerical results and measurements data is provided and discussed. By means of multi-stage unsteady computations is not only possible to accurately evaluate the aerodynamic performance, but also the harmonic content of the aerodynamic forcing functions on selected blade rows. Simplified computational approaches were investigated in order to assess their effectiveness and to reduce the computational resources. Design and off-design operating conditions have been investigated in order to evaluate the associated harmonic content of the forcing function.

In addition to the CFD simulations, the presented procedure also includes the FEM modal analysis of the blade row in cyclic symmetry. Blade row mode shapes are firstly used to compute the aerodynamic damping by means of an uncoupled flutter method. Finally, a modal work approach that takes as inputs blade mode shapes, aerodynamic damping and blade forcing is applied to obtain the forced response results in terms of vibrations displacements and stresses. A dedicated tool implements this modal work approach and the fist comparisons with aero-mechanical field data shows a good agreement taking the first encouraging step to the overall procedure validation.

Contents

Contents

Contents

List of Figures

List of Tables

Nomenclature

$\underline{C}$	Generalized damping matrix
$\underline{F}_{ext}(t)$	Generalized forcing vector
$\underline{K}$	Generalized stiffness matrix
$\underline{M}$	Generalized mass matrix
$\underline{n}$	Normal vector
$\underline{Q}$	Source terms vector
$\underline{U}$	Conservative quantities vector
$\underline{x}$	Generalized displacements vector
a	Speed of sound/Modal amplitude
A_0, A_n, B_n	Fourier series coefficient
b	Semi-chord
B	Blade
c	Absolute velocity/spouting velocity
C_p	Pressure coefficient
d	Scaling factor
E	Blade average kinetic energy
F_m	Modal force
FF	Flow function
h	Enthalpy/Harmonic index
i	Incidence angle
j	Imaginary unit
k	Scattering index
m	Circumferential order/modal mass
$\dot{m}$	Mass-flow rate
M	Mach number

Nomenclature

N	Number of sectors
NB	Blade count
p	Pressure
P	Power
r	radius
R	Degree of reaction/Gas constant
Re	Reynolds number
s	Entropy
T	Temperature/Torque/Period
t	Time
v	Relative velocity/y velocity component
w	Relative velocity/z velocity component
W	Specific work
Y	Total pressure loss coefficient

Greek Letters

α	Absolute flow angle/Phase
β	Relative flow angle
γ	Specific heats ratio
δ	Overall damping
ζ	Loss coefficient/Damping
η	Efficiency
θ	Circumferential direction
λ	Radii ratio
μ	Dynamic viscosity/Mass ratio
ν	Speed ratio/Excitation frequency
ξ	Kinetic energy loss coefficient/Critical damping ratio
ρ	Density
Σ	Blade surface
τ	Torque coefficient

Φ	Flow coefficient
$\underline{\Phi}$	Flux functions vector
Ψ	Stage loading
ω	Frequency/Specific Turbulent Dissipation
Ω	Rotational speed

Subscripts

0	Stagnation quantity
c	Corrected
is/ss	Isentropic
n	Natural
rel	Relative quantity
t	Turbulent
ts	Total-to-static
tt	Total-to-total
x	Axial

Acronyms

BC	Boundary Conditions
BPF	Blade Passing Frequency
BTW	Backward Travelling Wave
CA	Computational Aeroelasticity
CFD	Computational Fluid Dynamics
CFL	Courant-Friedrichs-Lewy number
CSD	Computational Solid Domain
DF	Diffusion Factor
DFT	Discrete Fourier Transform
EO	Engine Order
FEA	Finite Element Analysis
FEM	Finite Element Method
FRF	Frequency Response Function
FTW	Forward Travelling Wave

Nomenclature

GT	Gas Turbine
HCF	High Cycle Fatigue
HPT	High Pressure Turbine
IBPA	Inter-Blade Phase Angle
LCO	Limit Cycle Oscillations
LNG	Liquefied Natural Gas
LPT	Low Pressure Turbine
NGV	Nozzle Guide Vane
ND	Nodal Diameter
OMP	Open Multi-Processing
OP	Operating Point
PR	Pressure ratio
PS	Pressure Side
RANS	Reynolds-averaged Navier-Stokes
SS	Suction Side
TCF	Turbine Center Frame
TRF	Turbine Rear Frame
URANS	Unsteady Reynolds-averaged Navier-Stokes
ZZENF	Zig Zag Shaped Excitation Line

1 Introduction

Nowadays, the supply of the energetic market is increasingly wide, proposing solutions ranging from the exploitation of new renewable energy resources, to the use of sustainable alternative fuels (SAF) which allow to reduce the pollutant and the greenhouse gas (GHG) emissions. In this context, gas turbines play a strategic role as, unlike these new technologies, they are able to meet the peak of the global energy demand. They are the main source of power generation on the market thanks to their high flexibility and reliability, to the low operating costs, to the low emissions, to the high power density, and quality exhaust gases that can be further used for example in combined power plants and cogenerations processes.

Turbomachinery industries aim to design new machines with higher efficiencies but with lower risk of components failure to enhance their reliability. Since a trade-off design between these two aspects has to be found, turbomachinery blades are becoming lighter and more loaded, thus resulting more prone to aerodynamic excited vibrations. An accurate and detailed aeromechanical investigation of the engine modules is thus necessary during the design phase to prevent and to avoid any vibrations occurrence related to flutter and forced response phenomena. In this phase, the designer faces the vibration issues which involve various disciplines such as aerodynamics, solid dynamics, and aeromechanics. For this reason, all these disciplines need to be integrated into a single design procedure. Form a computational point of view, this approach is now possible thanks to the increase of computational power and to the performance of CFD

codes able to exploit the parallelism of modern HPC architectures. RANS analyses are the standard adopted by the industry, as they represent the optimal trade-off between computational cost and simulation accuracy. For aeromechanical assessment URANS simulations become necessary since they are essential to evaluate rotor/stator interactions and aerodynamic damping. Nevertheless, their huge computational cost can still be a limitation for the use of unsteady approaches in industrial routine design practice of turbomachines with a high stage count, as heavy-duty gas turbines.

1.1 Thesis objectives and outline

An integrated design considering both the aerodynamic and aeromechanic aspects of an axial gas turbine is becoming a great challenge for designers since it requires a tight bi-directional interaction of the different disciplines to avoid the occurrence of vibratory phenomena that can lead to undesired component failure. In order to reduce the iterations between the various design phases, and thus, the time-to-market, the development of this integrated procedure is a topic of particular interest.

The objective of this work is focused on the development of an integrated procedure for the aerodynamic and aeromechanic design of axial gas turbines blade rows. The methodology is based on steady and unsteady CFD simulations, which are used to evaluate the aerodynamic performance, aerodynamic damping and forcing functions which excite the turbine blade rows. On the other hand, FEM analyses are also needed to obtain natural frequencies and mode shapes, which are input data to calculate the aerodynamic damping (by means of flutter computations)

and the forced response analysis of the component under investigation.

After a general introduction about the fundamentals of axial turbine aerodynamic design, an overview of the main aeromechanical phenomena is provided. Chapter 2 describes the theory of a dedicated spatial decomposition of the forcing function generated by the stator/rotor interaction and the modal work approach algebra used to assess the forced response of blade rows.

The numerical methods adopted for CFD analyses are illustrated in Chapter 3. All the simulations have been performed with the CFD solver TRAF developed by the group of Prof. Arnone at the University of Florence. Concerning the flutter method, the two possible approaches, coupled and uncoupled, are explained.

Chapter 4 describes the workflow of the overall procedure, step by step, and its applications to the selected industrial test case: a LP turbine module of the Baker Hughes family, industrial partner of this activity. Two different operating points are investigated, the design and one off-design condition. Starting from the discretization of the fluid domain, the numerical setup for the multirow steady and unsteady analyses is presented. Two different numerical approaches are adopted, the Full-Navier Stokes and the inviscid endwall formulation analyses, in order to define an industrial strategy to reduce the computational cost of CFD analyses maintaining the required accuracy. Moreover, the instrumentation installed for the experimental test campaign, both for aerodynamic and aeromechanical measurements, is illustrated. The last part of the chapter presents the main steps for the forced response calculation and the numerical setup for all the unsteady flutter analysis.

All the numerical results obtained are discussed in Chapter 5. Firstly, steady state results for the two types of endwall treatments (viscous and inviscid) are compared to the unsteady ones and the available experimental data. Then, full annulus multi-stage unsteady results provide a detailed numerical solution of the flow field of the whole turbine domain, and two operating conditions are presented and compared. The harmonic content of the forcing function at single Blade Passing Frequency (*BPF*) is obtained with a dedicated post-processing which exploits the DFT in space and time of the pressure field. Finally, the predicted forced response value in terms of vibrating stresses is compared to measured field data. To obtain this value, the critical damping ratio curve is required and comes from an unsteady flutter analysis performed for all the even diameters. Looking at this curve, flutter stability for this blade row is also confirmed and further analyzed by showing the distribution of the energetic damping coefficient surface density over the blade for the different nodal diameter.

The concluding remarks and some future developments are finally reported in Chapter 6.

2 Fundamentals of Axial Turbine Aerodynamics and Aeromechanics

In this chapter, the fundamentals of aerodynamics and aeromechanics of axial gas turbines are reported. In the first part, an introduction of the machine operation and an overview of the principal layouts are presented. The main key parameters, used during the aerodynamic design phase of turbine stages, are analyzed to define the characteristics of an axial gas turbine. Then, a reinterpretation of the classical turbine maps by the definition of two new parameters is provided. Finally, blade cooling techniques are briefly discussed because of their impact on the aerodynamic design.

The second part deals with the aeromechanical design phase focusing on the two main phenomena: forced response and flutter. The phenomenology of these vibration occurrences is discussed, with a particular focus on its undesired effects in turbomachinery due to possible high cycle fatigue failure. Their different type of manifestation and basic theory equations will be provided as well.

2.1 Gas turbine

Gas turbine is a type of internal combustion engine in which burning of an air-fuel mixture produces hot gases that expand generating power. There are various configurations of that engine depending on the application, but the three main components are the:

2. Fundamentals of Axial Turbine Aerodynamics and Aeromechanics

- Air compressor module

- Combustion chamber

- Turbine module

A layout of a gas turbine engine is provided in Figure 2.1. The air flow is compressed by the axial compressor module and then introduced in the annular combustion chamber. Here, the air-fuel mixing takes place, thus increasing the temperature of the gas flow. Finally, the flow of hot pressured gases is expanded in the turbine producing torque used to generate shaft power or a propulsive force depending on the field of application.
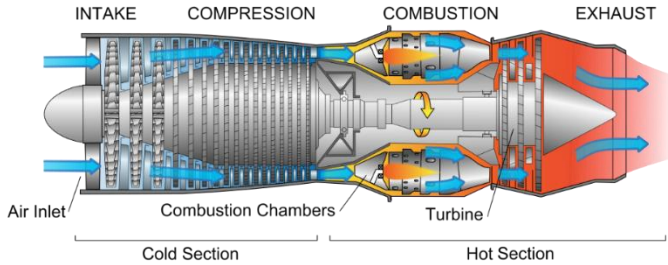
Figure 2.1: Gas turbine engine [1]

It is important to underline that in the gas turbine engine, the process of compression, combustion and expansion do not occur in a single component as they do in a reciprocating engine. These components are put in a row and therefore designed, tested, and developed individually and then linked together to form a gas turbine in a variety of configurations. In addition, other components, as heat exchanger, intercooling, etc. can be added to increase the power output and the efficiency of the plant. So, gas turbines are an extremely adaptable source of power and are used for a wide variety of applications, ranging

from electric power generation and jet propulsion to the supply of compressed air and process heat.

The thermodynamic process at the base of the gas turbine is the Joule-Brayton cycle that in its ideal form consists of two isobaric processes and two isentropic processes, as shown in T-s diagram in Figure 2.2 (right). The two isentropic transformations are the compression, 1-2s in T-s diagram, and the expansion, 3-4s in T-s diagram, carried out by the compressor and the turbine, respectively. The two isobaric transformations are the combustion process, from point 2,2s to point 3, which occurs in the combustion chamber and the heat rejection from point 4,4s to point 1.
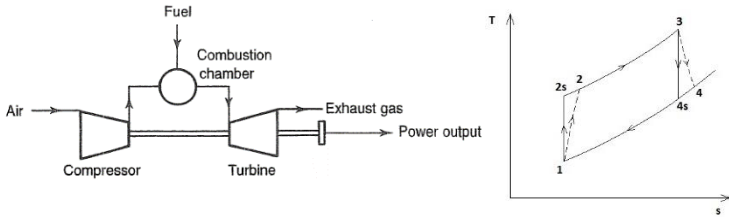
Figure 2.2: Simple gas turbine system (left) [2] and T-s diagram of reference Joule-Bryton cycle (right)

In Figure 2.2 is also provided a scheme of the plant that represent a *single-shaft* arrangement. This configuration is the most suitable if the gas turbine is required to operate at fixed speed and fixed load condition as in base-load power generation schemes. In a single-spool output shaft the output shaft is an extension of the main shaft which connects the compressor and turbine components. The output shaft may be an extension of the turbine shaft, "hot end drive" configuration, or it may be an extension of the compressor shaft, "cold end drive" configuration [3].

2. Fundamentals of Axial Turbine Aerodynamics and Aeromechanics

Flexibility of operation, e.g. the rapidity with which the machine can adapt itself to variation in load and rotational speed, is unimportant in this application. On the other hand, when flexibility in operation is required, the use of a mechanically free power turbine is desirable. In this case, the 1.5 shaft arrangement, called *twin-shaft*, is used (Figure 2.3). The high-pressure turbine drives the compressor and the combination acts as a gas generator for the low-pressure power turbine. The compressor-turbine shaft is not physically connected to the power output shaft, but it is coupled aerodynamically. This aerodynamic coupling is advantageous in that facilitates the start of the turbine components. Twin-shaft configuration may be used for electricity generation, with the power turbine designed to run at the alternator speed without the need for a reduction gearbox which represent a source of losses. Gas turbines originally designed for jet aircraft applications as turbojets, have been successfully adapted to ground based applications using the split output shaft configuration.
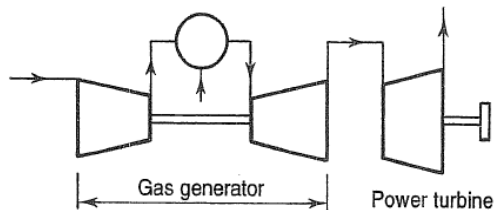
Figure 2.3: Gas turbine with separate power turbine [2]

For both single- and twin-shaft layout a relevant problem is an attempt to obtain high pressure ratio with only one compressor module. On way of overcoming this difficulty is to divide the compressor module into two or more components. This separation permits each section to run at a different rotational speed,

each with its own turbine. The low-pressure compressor is driven by the low-pressure turbine and the high-pressure compressor by the high-pressure turbine. Power is normally taken from the low-pressure turbine shaft, or from an additional free power turbine, Figure 2.4.
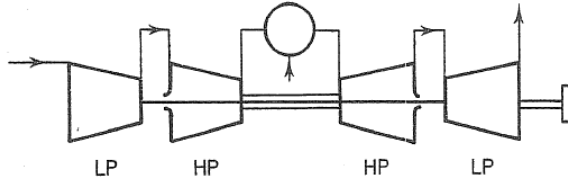
Figure 2.4: Twin-spool engine [2]

The configurations shown in Figure 2.4 is usually referred to as a *twin-spool* engine, with or without the free power turbine. It should be noted that although the two spools are mechanically independent, their speeds are related aerodynamically and thus designed together. As in the single spool configuration, the twin-spool arrangement was primarily developed for the aircraft engines, but there are many examples of aero-derivate turbines applied in the power generation field [4].

In addition to the type of arrangement, other classifications can be made for gas turbines [5]. Considering the origin of the machine, a distinction can be made between aero-derivative and heavy-duty gas turbines. This broad distinction is made for some main reasons. Firstly, the size and weight of an aero-derivative plant is much more compact than most other industrial applications of gas turbine. Secondly, aero-derivatives achieve higher compression ratios and efficiencies compared to the lowest heavy-duty ones, but they have a shorter life with a faster performance degradation. Lastly, the exhaust temperatures of the aero-derivatives gas turbines are relatively low compared to

the heavy-duty units. For this reason, their use in cogeneration or combined cycles is less attractive. These differences in the requirements can have a considerable effect on design and the realization of these machines. The aero-derivative turbines have to be adapted to the electrical generation industry by replacing the bypass fan with some compressor stages and adding a power turbine at the exhaust flange. These devices range in power from 2.5 MW to about 100 MW. The efficiencies of these units can range from 35-45%. On the other hand, heavy-duty gas turbines tend to be more like traditional steam turbines in their mechanical appearance than the lightweight constructions employed in aeronautical sector. In fact, restrictions of weight and space are not important factors for these ground-based units, and so the design characteristics include heavy-wall casing, large-diameter combustors, and blades without shroud, with low aspect ratio. These machines are the large power generation units ranging from 3 MW to 480 MW in a simple cycle configuration, with efficiency ranging from 30-46%.

The following section discuss about fundamentals of axial turbines design. The compressor and the combustor module are not described as they lie outside this thesis activity.

2.2 Turbine stage design

The turbine design starts from a two-dimensional analysis, called "mean-line analysis", which considers the variation of the flow along a mean radius through the machine. This is the simplest approach to the study of axial flow turbines which assume that the flow conditions prevailing at the mean radius fully represent the flow at all other radii. This two-dimensional analysis at the pitch line can provide a reasonable approximation to the actual flow, if the ratio of blade height to mean radius is small.

When this ratio is large, however, as in the final stages of an axial turbine a three-dimensional analysis is required.

2.2.1 Velocity diagrams

The axial turbine stage is composed by a row of fixed guide vanes or nozzle, called *stator* row, and a row of moving blades or buckets mounted on the rotor drum, called *rotor* row (Figure 2.5: Axial flow turbine stage). For a multi-stage turbine, the blading is arranged sequentially in an annulus with the disks connected via conical drive features forming the drum. The preliminary turbine design phase moves towards the decision of the stage velocity diagram, represented in Figure 2.5.
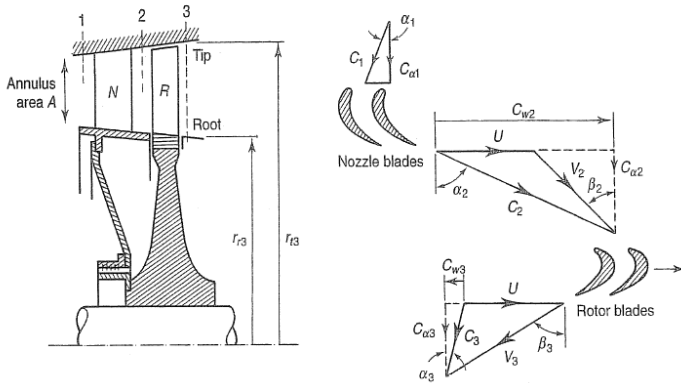
Figure 2.5: Axial flow turbine stage [2]

The flow enters the nozzle blades with absolute velocity c_1 at blade-to-blade angle α_1 and accelerates to an absolute velocity c_2 at an angle α_2, as shown in Figure 2.5. By vectorially subtracting the rotational speed U, the rotor inlet relative velocity w_2 with the direction β_2 is obtained. After being deflected, and further expanded in the rotor blade passage, the flow leaves with

velocity w_3 at an angle β_3. The relation between absolute, relative, and rotational speeds is expressed as:

$$\vec{C} = \vec{W} + \vec{U} \tag{2.1}$$

Because the blade speed U increases with increasing radius, the shape of the velocity diagrams varies from root to tip of the blade. For short blades, 2D mean flow design is valid but for long blades, 3D approach (which incorporates variations from hub to tip) must be adopted in design phase. At first, we shall consider the mean diameter of the annulus.

2.2.2 Design parameters

The following design parameters are used in the preliminary study of a repeating axial stage:

- Flow coefficient ϕ

- Stage loading ψ

- Degree of reaction R

The flow coefficient is defined as the ratio between the axial and the rotational speed, or,

$$\phi = \frac{c_x}{U} \tag{2.2}$$

The stage flow coefficient ϕ is a characteristic for the mass flow behaviour through the stage.

The second parameter is the stage loading ψ defined as the ratio between the total enthalpy rise per stage to the square of the rotational speed, or,

$$\psi = \frac{\Delta h_0}{U^2} = \frac{\Delta c_\theta}{U} = \frac{2c_x}{U}(\tan\beta_2 + \tan\beta_3) \qquad (2.3)$$

Since the turbine works with a "positive" pressure gradient, the boundary layer results more stable and tends to remain attached to the blade surface allowing the turbine designer to obtain higher stage loading values and larger flow turning than the compressor stages. However, locally on the blade suction side there could be a zone of an adverse pressure gradient depending on the turning and on the solidity of the blades. Thus, the boundary layer could grow rapidly or even separate in such a region affecting adversely the turbine efficiency. This region, called the diffusion region, is delimited by the minimum passage section or throat where the velocity is maximum. The diffusion factor parameter (DF) is introduced to support the stage load-ing choice, defined as follows [6]:

$$DF = \left[1 - \frac{c_2}{c_1}\right] + \frac{\Delta c_\theta}{2\sigma c_1} \qquad (2.4)$$

where σ is the turbine chord-to-pitch ratio. Diffusion in a tur-bine blade is usually around $DF \simeq 0.5$ and for high Reynolds number does not represent a design issue. Figure 2.6 illustrates the pressure distribution over the section surface depicting a zone of diffusion.
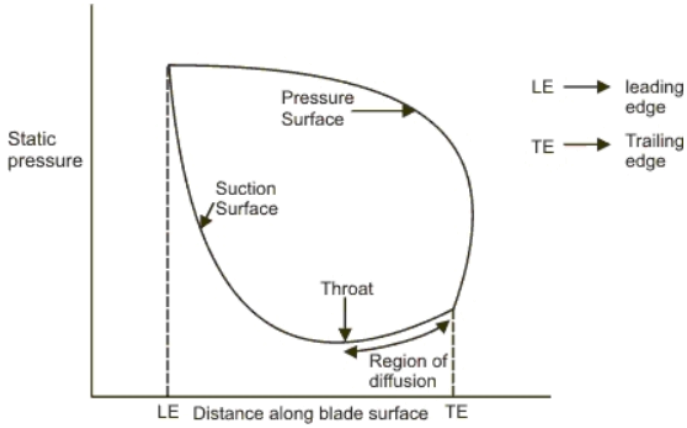
Figure 2.6: Turbine blade loading

Combining the equations of the blade loading and the flow coefficient, we obtain:

$$\psi = 2\phi \left(\tan\beta_2 + \tan\beta_3 \right) = 2\phi \left(\tan\alpha_2 + \tan\alpha_3 \right) \qquad (2.5)$$

The choice of these parameters must be made to ensure high efficiency for the stage. Maximum values of the efficiency are obtained for low values of the two coefficients.
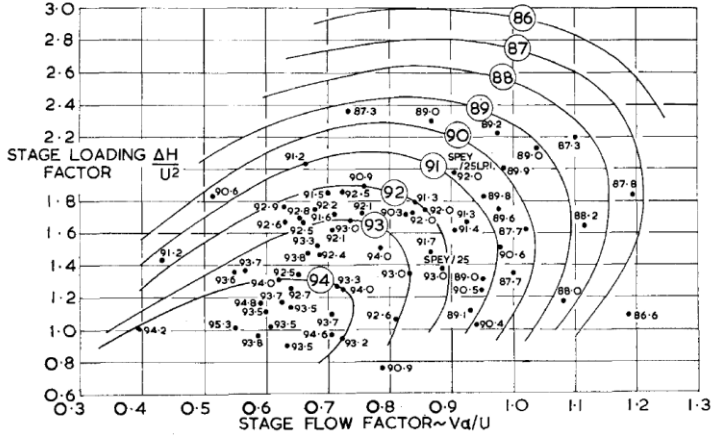
Figure 2.7: Smith diagram [7]

Furthermore, the degree of reaction R is defined as the ratio of the static enthalpy rise in the rotor to the static enthalpy rise in the stage, and it is usual to define it in term of static temperature or pressure drops rather than enthalpy drops, namely

$$R = \frac{h_2 - h_3}{h_1 - h_3} \tag{2.6}$$

The degree of reaction R indicates the portion of energy transferred in the rotor blading. Thus, after some mathematical passages, the Eq. (2.6) can be written as follows:

$$R = \frac{\phi}{2}(\tan \beta_3 - \tan \beta_2) \tag{2.7}$$

or,

$$R = 1 + \frac{\phi}{2}(\tan \alpha_3 - \tan \alpha_2) \tag{2.8}$$

and a compact relationship between the three designs parameter ϕ, ψ, R can be obtained:

$$\psi = 2\left(1 - R + \phi \tan \alpha_1\right) \tag{2.9}$$

This key parameter is fundamental for the blade geometry design as it describes the shape of the velocity triangles along the span. As previously explained, the blade tangential speed U and the velocity triangles are different from hub to tip section due to the radius variation along the blade spanwise direction (Figure 2.8). Thus, the stage loading and consequently the degree of reaction varies with it.
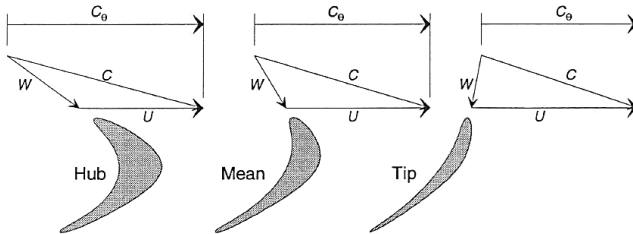
Figure 2.8: Velocity triangles at different spanwise positions

Low reaction rate values are desired near the hub section where high thickness and curvature profiles are required to minimize the centrifugal stresses action. Typical values of degree of reaction at the hub are around $R = 0.2 - 0.25$, necessary to provide a little pressure drop in order to overcome the endwall friction losses and make the flow expands within the hub rotor passage.

For midspan, a $R = 0.5$ is usually adopted. It corresponds to symmetrical triangles and a balance pressure drop between stator and rotor blades [8].

For tip section, high degree of reaction corresponds to thin blade profiles, beneficial to maintain low centrifugal stresses. Typical values for this case are about R = 0.65 – 0.7. Values over 0.7 are penalizing for the performance as they produce an increase of the tip clearance losses due to the flow leakage from pressure side to suction side. For this reason, where it is possible, shrouded blades are used to lower tip clearance losses, thus consequently increasing the aerodynamic performance by raising the stage reaction factor.

2.2.3 Stage losses and performance

The last step in the process of the preliminary design of a turbine stage is to check the loss coefficient and the stage efficiency. The estimation of the aerodynamic losses is important for the design process not only in the choice of the stage configuration, but also on the methods to control these losses. The choices of blade shape, aspect ratio, spacing, Reynolds number, Mach number and flow incidence angle can all affect the losses and hence the efficiency of turbine stages. Improving efficiency is associated with higher reaction, which implies less work per stage and therefore a higher number of stages for a given overall pressure ratio.

Two definitions of efficiency are commonly used, depending on the applications. The total-to-total efficiency (Eq.(2.10)),

$$\eta_{tt} = \frac{h_{01} - h_{03}}{h_{01} - h_{03ss}} \qquad (2.10)$$

defined as the ratio of the actual work output to the ideal work output when operating at the same back pressure. In the case the exit flow kinetic energy $\frac{1}{2}c_3^2$ cannot be recovered, a total-to-static efficiency better fits the stage performance:

$$\eta_{ts} = \frac{h_{01} - h_{03}}{h_{01} - h_{3ss}} \qquad (2.11)$$

The expansion process in turbine stage is illustrated in Figure 2.9.
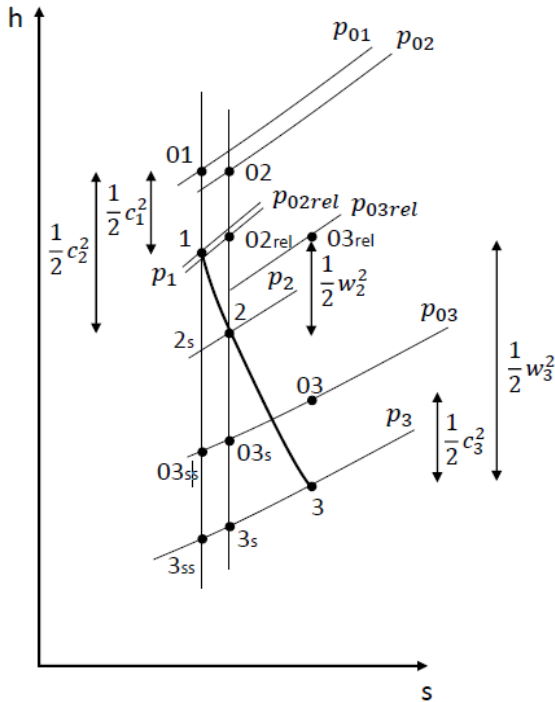
Figure 2.9: Mollier diagram for a turbine stage

In order to estimate the efficiency of a turbine stage as part of the preliminary design process, some methods of determining the loss coefficients is required. A classification of the principal sources of loss are summarized as follow [9]:

- Profile or primary losses

- Trailing edge thickness losses

- Secondary flow losses

- Trailing edge mixing losses

- Shock-waves losses

- Exit losses

From the Mollier diagram (Figure 2.9), losses are highlighted in terms of entropy rise and total pressure drop but different coefficients may be employed to evaluate losses during the preliminary design. For general considerations, a loss coefficient based on the increase in entropy can be expressed as follows [10]:

$$\zeta = \frac{T_2 \Delta s}{h_{02} - h_2} \qquad (2.12)$$

which refers to the expansion within the stator from state 1 to state 2 in the Mollier diagram.

This formulation is not very convenient when designing turbine rows and stages. For this reason, the total pressure loss is assumed as a measure of the entropy increase, and the total pressure loss coefficient is used [10]:

$$Y_p = \frac{p_{01} - p_{02}}{p_{01} - p_1} \qquad (2.13)$$

The same relationship may be also stated for the rotor row by switching to the relative properties. Another coefficient used during the design phase is the kinetic energy loss coefficient [10], expressed as:

$$\xi = \frac{h_2 - h_{2s}}{h_{02} - h_2} \qquad (2.14)$$

The previous equation, valid for a stator row, may be extended to the rotor by substituting the absolute with relative quantities. Several correlations to estimates losses and the way they influence aerodynamic efficiency have been investigated over the years. Horlock [11], Craig and Cox [12], Kacker and Okapuu [13], and Ainley and Mathieson [14] are just some of those who have published correlations and scientific papers about this topic. For 2D losses, experimental cascades are usually adopted. The three-dimensional effects, such tip leakages, exit flow mixing and secondary flows impact to the overall performance decrease. In a preliminary design, they may be accounted for using some coefficients previously mentioned. Nevertheless, fully 3D CFD analyses must be carried out to ensure accurate results for the blade design.

2.2.4 Turbine maps

Because the gas turbine performance varies significantly from one operating point to the other, the procedure to determine the performance of single-stage or multistage axial flow turbine for a specific operating point is to use the performance maps. To

define such engine performance maps, the similarity theory can be introduced.

Turbomachines can be compared with each other by dimensional analysis with the Buckingham theorem [15]. This analysis is a procedure where variables representing a physical situation are reduced into groups, which are dimensionless. These dimensionless groups can then be used to compare performance of various types of machines with each other. In turbomachines, dimensional analysis is employed to compare data from various types of machines, to select various types of units based on maximum efficiency and pressure head required, and to predict a prototype performance from test conducted on a smaller scale model or at lower speed. Buckingham's Pi theorem states that if there are n variables in a problem and these variables contain m primary dimensions (for example mass, length, time) the equation relating all the variables will have $(n\text{-}m)$ dimensionless groups.

The performance parameters, the total-to-total isentropic enthalpy drop/rise $\Delta h_{tt,is}$, the isentropic efficiency $\eta_{tt,is}$, and the power P can be expressed functionally as:

$$\Delta h_{tt,is} = f\left(\mu, N, D, \dot{m}, \gamma, a_{01}\right) \qquad (2.15)$$

$$\eta_{tt,is} = g\left(\mu, N, D, \dot{m}, \gamma, a_{01}\right) \qquad (2.16)$$

$$P = j\left(\mu, N, D, \dot{m}, \gamma, a_{01}\right) \qquad (2.17)$$

2. *Fundamentals of Axial Turbine Aerodynamics and Aeromechanics*

Starting from these independent dimensional parameters, various independent dimensionless groups can be obtained. Among these:

1. The Reynolds number

$$Re_D = \frac{p_{01}ND^2}{RT_{01}\mu} \tag{2.18}$$

2. The corrected speed

$$N_c = \frac{ND}{a_{01}} \tag{2.19}$$

3. The non-dimensional enthalpy drop/rise

$$h_s = \frac{\Delta h_{tt,is}}{a_{01}^2} \tag{2.20}$$

4. The flow function

$$FF = \frac{\dot{m}\sqrt{RT_{01}}}{\rho_{01}a_{01}D^2} \tag{2.21}$$

In this way, selecting as common factors N, D, p_{01}, and T_{01}, the performance parameters $\Delta h_{tt,is}$, $\eta_{tt,is}$, and P may be reduced to five dimensionless groups:

$$\frac{\Delta h_{tt,is}}{N^2D^2}, \eta_{tt,is}, \frac{P}{\rho_{01}N^3D^5} = f\left(\frac{\dot{m}}{\rho_{01}ND^3}, \frac{\rho_{01}ND^2}{\mu}, \frac{ND}{a_{01}}, \gamma\right) \tag{2.22}$$

After some algebra, the isentropic enthalpy drop, and the power coefficient can be conveniently expressed as

$$\frac{\Delta h_{tt,is}}{a_{01}^2} \propto f\left(\frac{p_{02}}{p_{01}}\right) \qquad (2.23)$$

$$\frac{P}{\rho_{01} N^3 D^5} \equiv \frac{\Delta T_0}{T_{01}} \qquad (2.24)$$

Collecting all these newly formed non-dimensional groups and inserting them in Eq. (2.22) gives

$$\frac{p_{02}}{p_{01}}, \eta_{tt,is}, \frac{\Delta T_0}{T_{01}} = f\left(\frac{\dot{m}\sqrt{RT_{01}}}{p_{01}D^2}, \frac{ND}{\sqrt{RT_{01}}}, Re_D, \gamma\right) \qquad (2.25)$$

For a machine of a specific size and handling a single gas it has become customary to delete γ, R, and D from Eq. (2.25). If, in addition, the machine operates at high Reynolds numbers (or over a small speed range), Re can also be dropped. Under these conditions Eq. (2.25) becomes

$$\frac{p_{02}}{p_{01}}, \eta_{tt,is}, \frac{\Delta T_0}{T_{01}} = f\left(\frac{\dot{m}\sqrt{T_{01}}}{p_{01}}, \frac{N}{\sqrt{T_{01}}}\right) \qquad (2.26)$$

Then, whether calculated, or measured on a test rig, the performance is normally expressed by plotting η_{tt} and $\dot{m}\sqrt{T_{01}}/p_{01}$ (Figure 2.10) against expansion ratio p_{02}/p_{01} for various values of $N/\sqrt{T_{01}}$.
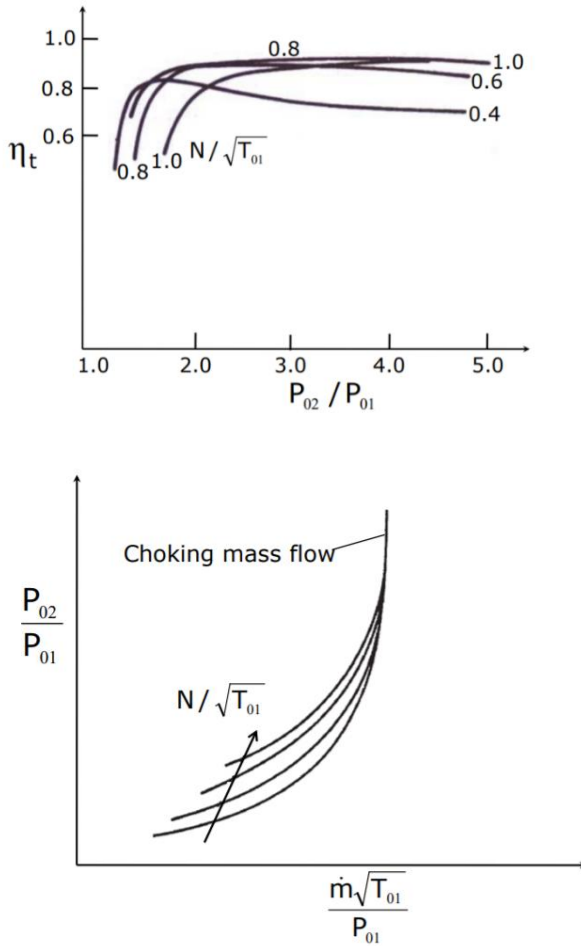
Figure 2.10: Turbine characteristics: total-to-total efficiency (top) and flow function (bottom)

The efficiency plot shows that η_{tt} is sensibly constant over a wide range of rotational speed and pressure ratio. This is because the accelerating nature of the flow permits turbine blading

to operate over a wide range of incidence without much increase in the loss coefficient. The maximum value of mass flow rate is reached at a pressure ratio which produces choking conditions at some point in the turbine. Choking may occur in the nozzle throat or in the annulus at outlet from the turbine depending on the design. The former is the more normal situation and then the constant speed lines merge into a single vertical line independent of speed, as indicated on the mass flow plot. Unlike the compressor characteristics, in turbines the flow is generally from high pressure to low, and there are no regions of unstable flow in a turbine characteristic map.

With this formulation, the characteristics curves are difficult to interpolate and to read due to lines crossing. In order to simplify reading and improve its use, it is possible to express the selected performance parameters, flow function and isentropic efficiency, in terms of another quantity [16]. Isentropic enthalpy drop $\Delta h_{tt,is}$ and corrected speed N_c can be combined in a single variable, the speed ratio ν:

$$\nu = \frac{U}{\sqrt{2\,\Delta h_{tt,is}}} = \frac{\dfrac{U}{a_{01}}}{\sqrt{2\dfrac{\Delta h_{tt,is}}{a_{01}^2}}} = \frac{N_c}{\sqrt{2\,h_s}} \tag{2.27}$$

where U is the blade velocity at midspan and the square root of twice the isentropic enthalpy drop is sometimes referred to as "spouting velocity", $c_{is} = \sqrt{2\,\Delta h_{tt,is}}$, the velocity of a gas expanding isentropically in a nozzle working under an isentropic total-to-static enthalpy drop equal to $\Delta h_{tt,is}$.

Moreover, turbine maps are traditionally plotted versus the expansion ratio (p_{02}/p_{01}). As previously shown, stage performance can be expressed as a function of p_{02}/p_{01} and γ or, alternatively, of h_s and γ. However, in the second case, the fact that h_s itself depends on γ reduces considerably the residual explicit influence of γ. For this reason, expressing performance in terms of h_s instead of p_{02}/p_{01} has a more general validity. So, the isentropic efficiency and flow function (FF) curves can be expressed in terms of h_s and v instead of h_s and N_c:

$$FF = f\ (h_s, N_c) \rightarrow FF = f'\ (h_s, v) \tag{2.28}$$

$$\eta_{tt,is} = g\ (h_s, N_c) \rightarrow \eta_{tt,is} = g'\ (h_s, v) \tag{2.29}$$

These new relationships allow to show the maps a new trend. The efficiency curves tend to collapse on each other (Figure 2.11). This factor indicates that performance does not depend on the pressure ratio and speed separately, but on a combination of them, as long as the operating conditions remain subsonic. On the other hand, flow function has still a strong dependency on pressure ratio. However, curves do not cross anymore. The h_s and v values are shown in a non-dimensional form. The superscript * indicates a reference value.
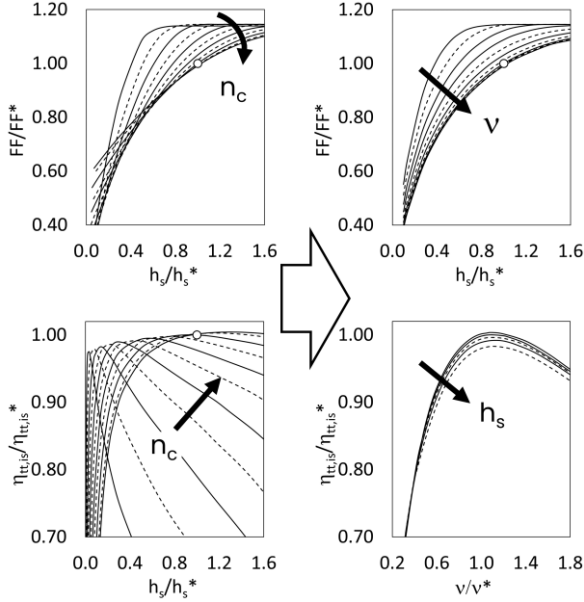
Figure 2.11: Flow function (top) and efficiency (bottom) maps transformed with the change of variables from h_s and n_c (left) to h_s and v (right) [16]

A physical interpretation of these parameters has been given considering a turbine stage. In addition, similar considerations can be applied to multistage turbines. The physical interpretation of these maps is linked to the effect of the speed ratio on incidence. In fact, if we look at the distributions of pressure coefficient C_p along a blade profile at midspan for different operating conditions, imposing the non-dimensional isentropic enthalpy drop while varying the velocity ratio corresponds to keeping the same location and value of peak suction C_p on the airfoil and changing only the approaching flow incidence (Figure 2.12). In particular, the incidence increases as the velocity ratio decreases, while it becomes negative for high values of v/v^*.
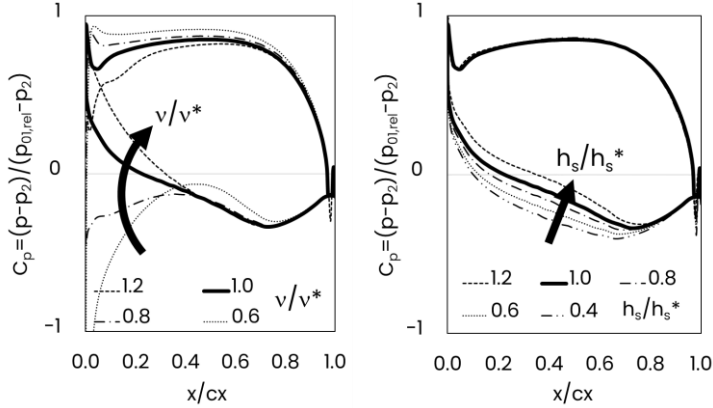
Figure 2.12: Distributions of pressure coefficient C_p along the blade profile. Left: velocity ratio v/v^* is varied while non-dimensional isentropic enthalpy ratio h_s/h_s^* is fixed. Right: h_s/h_s^* is varied while v/v^* is fixed [16]

On the contrary, at fixed velocity ratio, illustrated in the right plot, the incidence angle remains unchanged whatever the pressure ratio is. The changes in the latter affect the location and the value of peak suction C_p. Similar considerations still apply when the pressure ratio is changed at velocity ratios different from the design value. In summary, Figure 2.12 confirms the distinct role played by h_s and v and it clarifies their orthogonal relationship and corresponding impact on the aerodynamic load of the blade.

Moving into a deeper insight of the flow physics, plots in Figure 2.13 and Figure 2.14 provide a visual confirmation of what just discussed and confirm that in a turbine stage incidence and compressibility effects are governed by h_s and v independently. They report respectively C_p and Mach number contours of a blade at midspan for different values of v/v^* at $h_s/h_s^*=1.0$, see

Figure 2.13, and for increasing levels of h_s/h_s^* at $\nu/\nu^*=1.0$, see Figure 2.14.
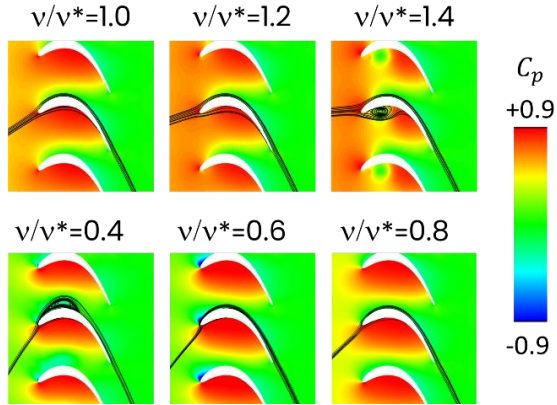
Figure 2.13: Streamlines at midspan and contours of pressure coefficient C_p for different ν/ν^* at $h_s/h_s^*=1.0$. Incidence is changed from positive ($\nu/\nu^*<1$) to negative ($\nu/\nu^*>1$), while levels of C_p remain substantially unchanged [16]
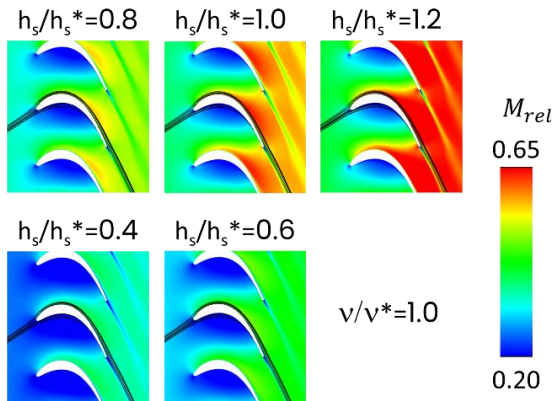
Figure 2.14: Streamlines at midspan and contours of relative Mach number M_{rel} for different values of h_s/h_s^* at $\nu/\nu^*=1.0$. Levels of M_{rel} change at fixed incidence [16]

The relationships between incidence ι and v/v^*, as well as between isentropic relative Mach number at blade outlet, $M_{2,rel,is}$, and h_s/h_s^* are illustrated in Figure 2.15.
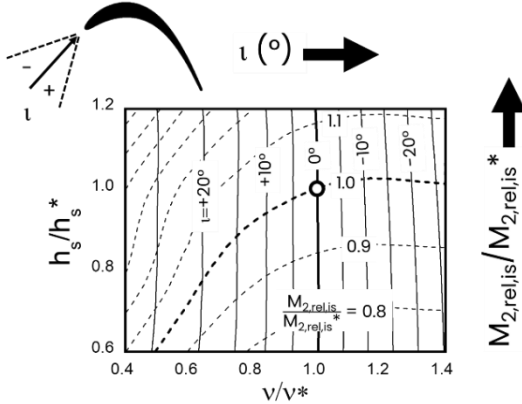
Figure 2.15: Incidence (ι) and exit isentropic relative Mach number ($M_{2,rel,is}$). Dashed lines correspond to Mach number ratio $M_{2,rel,is}/M_{2,rel,is}^*$, solid lines correspond to incidence angle ι [16]

Any couple of values (v/v^*, h_s/h_s^*) is in one-to-one relationship with a corresponding combination of values of ι and $M_{2,rel,is}/M_{2,rel,is}^*$. More specifically, the velocity ratio is in one-to-one relationship with the incidence on the blade, so that in practice v/v^* is constant along the lines at fixed incidence ι. As far as the lines of constant isentropic relative Mach number are concerned, instead, they tend to drop in the plane, h_s/h_s^*-v/v^* as the velocity ratio decreases. In other words, at fixed h_s/h_s^* the $M_{2,rel,is}/M_{2,rel,is}^*$ increases as v/v^* decreases. On the other hand, moving to the right, this trend is inverted and $M_{2,rel,is}/M_{2,rel,is}^*$ decreases at constant h_s.

2.2.5 The torque maps

Another performance parameter is the specific torque coefficient, defined as it follows Eq. (2.30):

$$\tau = \frac{T}{\dot{m}\, r\, \sqrt{2\, \Delta h_{tt,is}}} \tag{2.30}$$

in which r is the blade radius at midspan and T is the torque measured by the torque-meter. The torque coefficient can be defined at any operating point and it is linked to the isentropic efficiency through the following relationship:

$$\tau = \frac{\eta_{tt,is}}{2\, \nu} \tag{2.31}$$

As a result, the torque coefficient could in principle replace the isentropic efficiency as the overall performance parameter.
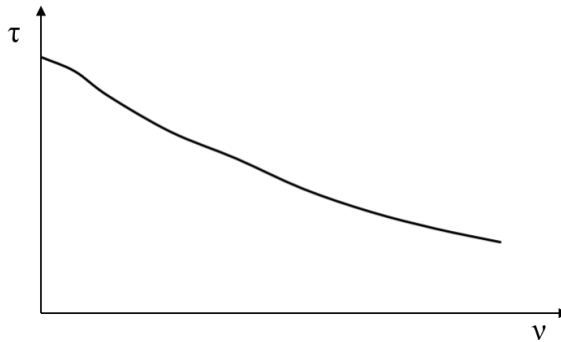
Figure 2.16: Torque coefficient curve

2. Fundamentals of Axial Turbine Aerodynamics and Aeromechanics

Thanks to the Euler's equation, the expression of torque coefficient of Eq. (2.31) and Eq.(2.30) for a single stage turbine, can be further developed into Eq. (2.32) [16]:

$$\tau = \frac{T}{\dot{m}\, r\, c_{is}} = \frac{c_{1u}u_1 - c_{2u}u_2}{u_1 c_{is}} =$$

$$= \left(\frac{c_1}{c_{is}}\right) sin\alpha_1 + \lambda \left(\frac{w_2}{c_{is}}\right) sin\beta_2 - \lambda^2 v = \qquad (2.32)$$

$$= \mu(h_s, v) - \lambda^2 v$$

where λ is the ratio between the midspan radii at different locations and where c_1, w_2 and α_1, β_2 are respectively the absolute and relative velocities at stator and rotor exit and the absolute and relative flow angles (measured from the axial direction) at the same locations. The structure of the equation suggests a strong, explicit dependency on the velocity ratio v: for a fixed pressure ratio (i.e. h_s), the torque coefficient decreases as the velocity ratio increases. This physically happens because the residual absolute tangential velocity at rotor exit, c_{2u}, increases with v, thus reducing the torque developed by the rotor for a given incoming absolute swirl velocity c_{1u}. Of course, also h_s influences τ, through the term $\mu(h_s, v)$. Nevertheless, the dependency on the pressure ratio of c_1/c_{is}, w_2/c_{is} and of α_1, β_2 is moderate, provided that incidence is not excessive. Concluding, stage efficiency from Eq. (2.29) and Eq. (2.31 can be written as:

$$\eta_{tt,is} = 2v[\mu(h_s, v) - \lambda^2 v] \qquad (2.33)$$

which confirms the very strong relationship between efficiency $\eta_{tt,is}$ and velocity ratio v.

For mechanical drive applications an accurate prediction of the starting torque is very important. For instance, if the load is a compressor (like in LNG applications), the possibility to start from pressurized conditions depends on the torque developed by the turbine when the rotor is locked.

2.3   Gas turbine cooling

In the gas turbine industry, there has been a continuing trend towards higher turbine inlet temperature in order to maximize the efficiency of gas turbine engines. This trend has been made possible by advancement in materials and technology, and the use of advanced turbine blade cooling techniques. In fact, increasing the turbine inlet temperature affects the thermal efficiency and, at such high thermal loadings, the heat transfer to the turbine blades increases. The gas temperature can reach the thermal limits of the turbine blade materials resulting in blade oxidation and potential blade destruction by melting.

To prevent these phenomena, various methods has been used to protect the turbine components exposed to the hot gases Figure 2.17 shows the various cooling techniques used to safely operate a turbine blade at high temperatures.
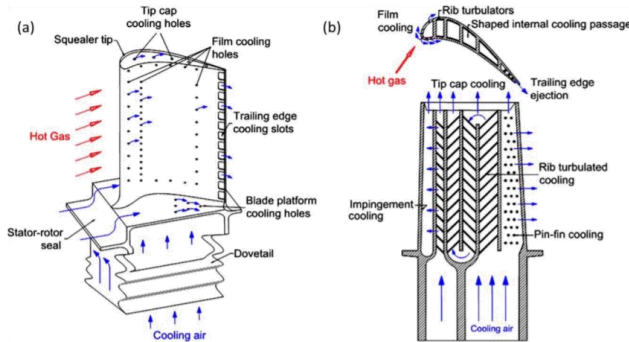
Figure 2.17: Gas turbine blade cooling techniques. External (a) and internal (b) cooling [17]

Typically, cooling is provided by extracting some compressed air and by-passing the combustion chamber directly into the turbine. Two main types of cooling techniques have been developed, internal and external cooling. The most common are internal convection cooling, like, impingement, turbulated multipass serpentine passages, flow through pin-fin arrays or simply smooth or turbulated radial channels. On the other hand, the external cooling allows air cooling from inside the blade to eject out onto the hot-gas side surface through discrete holes, creating a small layer that protect the blade. Other means of protecting gas turbine blade include using thermal barrier coatings. This coating are materials applied to the surface of the blade to protect it from effects of the high temperature environment, like oxidation and corrosion. So, basically, a combination of the various cooling methods available is used to achieve the best cooling performance for the gas turbine blade. However, a balance has to be maintained when employing the cooling methods because the extraction of the cooling air from the compressor adversely affects the overall gas turbine efficiency, since work has been done on the fluid to compress it. Also, addition of coolant back

into the hot gas stream results in further thermodynamic penalties. To optimize the overall thermal efficiency of a gas turbine engine, there is a need to properly evaluate the overall performance of any cooling configuration.

In addition, to understand the cooling requirements of a gas turbine blade, an understanding of the aerodynamic and heat transfer principles guiding the flow through the gas turbine blade passages is required. It is necessary to study these principles in the various regions of the gas turbine blade to maximize the cooling performance as temperature may vary along the blade surface from leading to trailing edge by 200 to 300 K. Furthermore, competence in material characteristics and selection is needed. Turbine blades and nozzles are commonly formed by investment casting. This process allows the alloy to acquire its crystalline structure, which is a major determinant of the properties of the finished part. Casting technology has advanced further, towards unidirectional solidification and even the casting of blades as a single crystal. Thanks to the latter, the material resistance to creep, to high-frequency vibration fatigue stresses and, to low-frequency thermal fatigue stresses is increased.

2.4 Aeromechanical design

As stated in the preliminary aerodynamic design, axial machines have relatively thin blades, but with high aerodynamic loads. This leads to a possible increase of vibratory phenomena onset. So, after an aerodynamic design phase, which is fundamental for the evaluation of the performance of gas turbine engines, an aeromechanical investigation has to be carried out to identify all the possible vibration issues that may compromise blade-rows integrity.

2. Fundamentals of Axial Turbine Aerodynamics and Aeromechanics

In turbomachinery environment, aeromechanical problems are mainly due to the interaction between the components and the surrounding fluid flow. The discipline that studies these interactions is called aeroelasticity. This science concerns the study of static and dynamic interactions between aerodynamic, elastic, and inertial forces acting on a flexible structure and the phenomena that can result. The interdisciplinary nature of the field is clearly summarized by Collar's diagram (Figure 2.18) which represents the connections between dynamics, fluid mechanics and structural mechanics [18] [19].
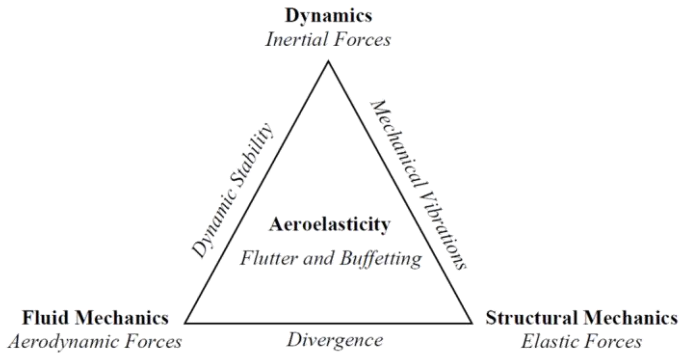
Figure 2.18: Collar triangle

The three disciplines in Collar's diagram are related to the dynamic equation shown below:

$$\underline{M}\,\ddot{x} + \underline{C}\,\dot{x} + \underline{K}\,x = \underline{F}_{ext}(t) \tag{2.34}$$

where M, C and K are the mass, damping and stiffness matrices respectively, $F_{ext}(t)$ contains the aerodynamic forces acting on the structure and x denotes the vector of displacements. Solving the Eq. (2.34) with $F_{ext}(t) = 0$, it is possible to obtain the blades eigenfrequencies and the mode shapes of the system. In fact, as

any other structure, each bladed disk has eigenfrequencies asso-
ciated with mode shapes which can be considered as a combina-
tion of disk-alone and blade-alone mode shape. Blade modes are
usually classified depending on the number of inflection lines
(1st, 2nd, etc.) and their orientation with respect to the blade
(bending or flexion F, torsion T, etc.). In general, the low fre-
quency blade mode shapes are 1st bending (1F), 1st torsion (1T)
and 2nd flexion (2F). Considering the cyclic structure as a disk,
each mode shape family is composed by n vibration traveling
waves defined by the Nodal Diameters (ND) value. An example
of a representations of nodal diameter is illustrated in Figure
2.19.
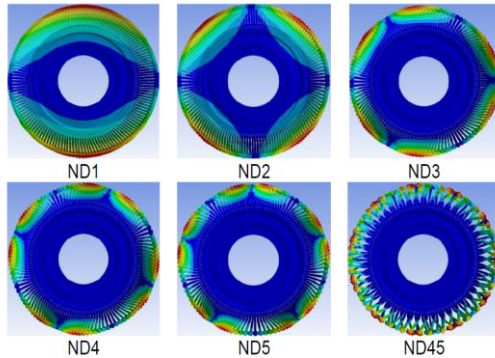
Figure 2.19: Nodal diameters representation [20]

Nodal diameters represent the diametrical lines which connect
the zero displacements nodes, while the structure is vibrating.
The ND maximum value that a bladed disk can have is limited
by the maximum number of possible axisymmetric divisions and
consequently related to the blade count and, in particular, is
N/2 for an even number of sectors and (N − 1)/2 for an odd
number of sectors. For each travelling wave, the blades vibrate
at a single blade mode shape, frequency, and amplitude, but

with a phase shift between adjacent profiles defined by the parameter Inter-Blade Phase Angle (IBPA):

$$IBPA = \frac{2\pi}{N} n \ \ with \ n \in Z: \ -\frac{N}{2} \le n < \frac{N}{2} \qquad (2.35)$$

where n is the number of nodal diameter and N is the number of sectors. The sum of all phase angles along the blade row must be 2π or its multiple. The sign of the travelling wave is established according to the IBPA:

- If IBPA > 0, the lower blade is in phase advance and the travelling wave propagates in backward direction

- If IBPA < 0, the lower blade is in phase delay and the travelling wave propagate in a forward direction.

According to "tuned" row assumption, all blades are identical to each other in terms of geometrical and mechanical properties within a bladed disk [21]. A sector of one blade plus the corresponding tangential segment of the disk in a tuned disk composed of N identical angular sectors is shown in Figure 2.20. The single sector can be analyzed with the cyclic symmetry approach instead of studying the entire wheel.
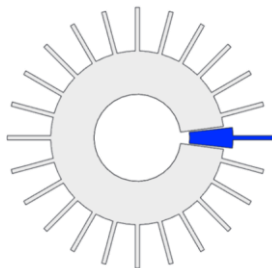
Figure 2.20: Cyclic symmetry

By applying the boundary conditions at the tangential cuts with adjacent angular sectors, a model of just one sector is sufficient to predict the vibration of the entire cyclic structure. This is not exactly what really happens in an actual turbomachine. Blades are not identical each other due to manufacturing differences which can lead to small property discrepancies between different blade angular sectors of the same blade row. Moreover, different blade-disk connections are possible such as fir-tree or dove tail attachments. Rotor blades are often welded to the disk or even produced as integral part of both disk and blade (blisk). For this reason, different trends of natural frequencies can be observed considering the disk-alone mode shapes family rather than blade-alone family, rather than bladed disk family.
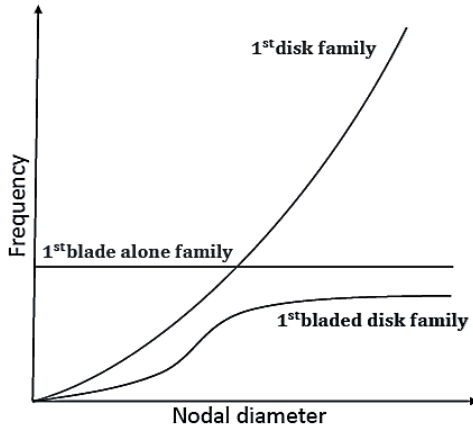
Figure 2.21: Blade-alone, disk-alone and bladed disk frequency curves

Figure 2.21 shows how blade-alone modes have a constant frequency that does not depend on nodal diameter number as the adjacent blade coupling due for instance to the disk very low.

2. Fundamentals of Axial Turbine Aerodynamics and Aeromechanics

On the other hand, whin maximum coupling occurs, the disk-alone frequencies increase with nodal diameter number. Finally, disk and blade modes are present in a bladed disk family: at low frequencies, the trend of the curve is similar to the disk modes, while increasing in frequency, blade-alone modes dominate due to the less participation of blade connectors (disk, shroud, etc.). The mode shapes obtained from the analysis can be defined as real mode shapes or complex mode shapes. The characteristic of a real mode shape is that all the point displacements in the structure are in phase or out of phase with respect to any other points in the structure. However, in complex mode shapes the point displacements in the structure are neither in phase nor out of phase with any other point in the structure.

After this brief introduction on the aeroelasticity theory and the blade row vibration, the focus moves on the design method for two main aeroelastic phenomena in turbomachinery applications: forced response and flutter. The key elements of an analytical design system are shown in Figure 2.22.
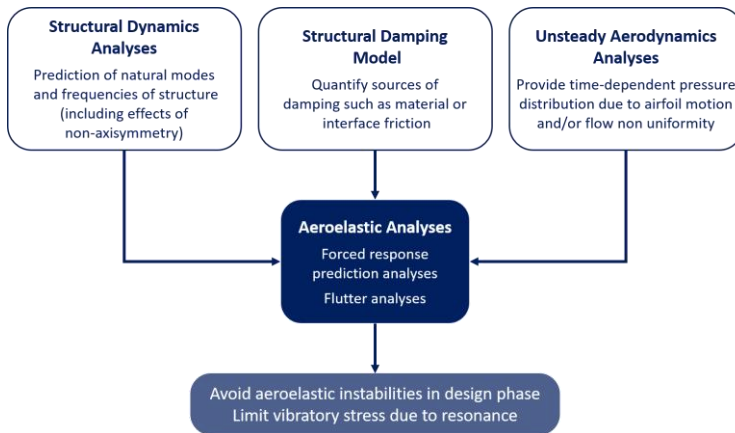
Figure 2.22: Aeroelastic design analyses [22]

The aim of this approach is to predict forced response or flutter onset on turbomachinery components to eliminate high cycle fatigue failure in the design phase. These design systems are largely centered on defining the sources and/or mechanism of forcing function generation and accurately predicting the aero-elastic properties of the component.

2.4.1   Forced response design

Forced response vibration belong to the family of synchronous oscillations which occur when periodic flow disturbances pass through the blade passages, resulting in an unsteady pressure field acting on the blade surface. The aerodynamic excitation forces are primarily due to:

- Circumferential flow distortions, normally caused by blades passing through the wakes of upstream rows

- Upstream and downstream rows potential interaction

- Non-uniform inlet flow in terms of pressure, temperature, and velocity due to injections/extractions

- Back pressure fluctuations

Potential resonant conditions occur when the aerodynamic forcing frequency of the incoming flow disturbances coincides with the blade mode natural frequency. In this condition, the forced vibration response can reach particularly high levels, causing ultimately the failure of the blade due to the so-called High Cycle Fatigue (HCF). Frequency resonances are commonly identified using the Campbell diagram, shown in Figure 2.23.
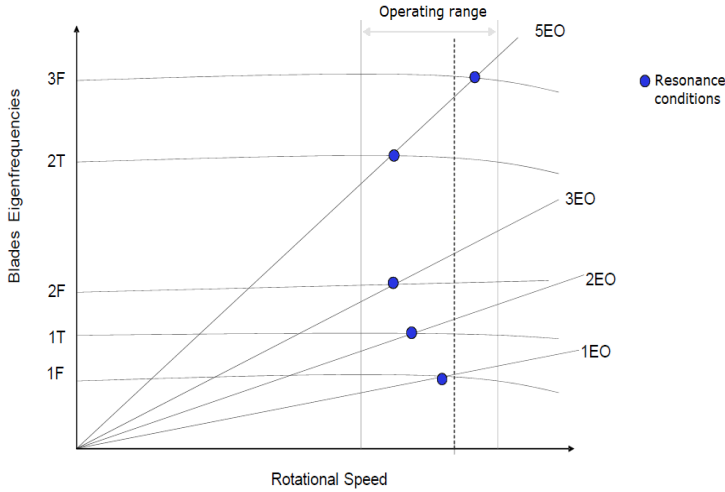
Figure 2.23: Campbell diagram [**23**]

In this diagram for a rotor row, blades eigenfrequencies are represented as function of the rotor speed for different engine order excitations. The engine order excitation frequency or its multiples are defined as:

$$\nu_{EO} = \frac{\Omega \cdot EO}{2\pi} \qquad (2.36)$$

where ν is the excitation frequency in sec^{-1}, Ω is the rotational speed in rpm and EO is the engine order.

Generally, blade natural frequencies of a rotor row tend to increase as rotational speed rises as a consequence of the centrifugal stiffening, as reported in Figure 2.23. In turbine, there can be also a slight reduction in natural frequency as speed increases due to the increased temperature that causes creep phenomenon.

The Campbell diagram can either be obtained analytically from a finite element analysis (FEA) or experimentally by a forced response tests in a rotating engine using strain gauges placed on the blades. In blade design, the Campbell diagram is used to place natural frequencies crossing either above the maximum engine speed or below the normal operating range with the aim of avoiding continuous resonant excitation during operation. However, crossing points at speeds below the operating range are always encountered during the start-up and shut down of each operational cycle, resulting in resonant vibration contributing to HCF. Since all the resonances in turbomachines cannot be avoided, the vibration levels at all encountered crossing points must be evaluated to determine the risk of fatigue failure during the service life of the machine.

The Campbell diagram shows only the possible crossing frequency information and it is valid only for a single nodal diameter. When the blade eigenfrequencies vary with nodal diameter, the Zig-Zag shaped Excitation line in the Nodal diameter versus Frequency (ZZENF) diagram is adopted [24] [25]. In this diagram, natural frequency variation as a function of the nodal diameter is taken into account simultaneously. The ZZENF diagram is an interference diagram particularly useful for evaluating which engine order causes the resonance condition for a certain nodal diameter within a blade row mode family. Resonant conditions for a rotationally periodic structure are when natural frequencies match the following relationship:

$$\omega_n = (kN \pm n)\Omega \qquad (2.37)$$

with $k = 0,1,\dots,N$, where ω_n is the natural frequency, N is the number of blades sectors and n the nodal diameter. Only intersections at integer values of n lead to a resonance condition and

the system response is a foreward or a backward travelling wave with respect to the rotor rotational speed according to whether the crossing happens when the line of the rotational speed is ascending $(kN + n)\Omega$ or descending $(kN - n)\Omega$. Figure 2.24 shows an example of a ZZENF diagram built for an axial turbine row of 60 blades in which it is possible to identify where resonances could potentially occur on the natural frequency curves, connecting each engine order to a corresponding nodal diameter.
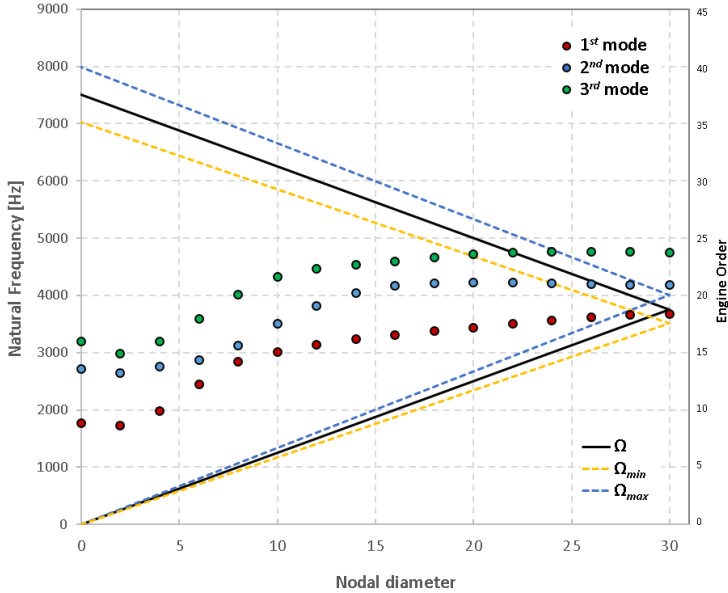
Figure 2.24: ZZENF diagram

The analysis is usually focused on a set of specific engine orders that describe blade counts, found through a DFT analysis of the aerodynamic loading. The travelling wave propagation direction is also predictable by checking the zig-zag versus, highlighted by the black line in the plot. In order to specify the frequencies

that will be excited by each engine order when the turbine is running, further zig-zag lines have been added above and below the line representing the design speed Ω. These specify an interval according to the entire speed range plus a safety margin between Ωmin and Ωmax.

2.4.2 Spatial decomposition

To apply the theoretical concepts described in the Zig-Zag diagram and to assess the forced response of a cyclic system it is necessary to implement a dedicated spatial decomposition of the unsteady forcing generated by rotor/stator interactions. The overall unsteady pressure on blade surfaces of a single row, coming from unsteady analysis as a set of instantaneous solutions within a discretized period, must be decomposed before studying the blade mechanical response by means of the modal approach at the Zig-Zag crossings. The pressure signal decomposition is performed by using the Discrete Fourier Transform (DFT), applied both in time and in space, to extract the pressure fluctuation components in the cyclic symmetry environment. This means that the time-varying pressure fluctuation seen by an airfoil row is firstly decomposed in time to extract the harmonic content at a single Engine Order (EO) by the following formulation:

$$P^{(h)} = \frac{1}{N_{div}} \sum_{n_t=0}^{N_{div}-1} p_t \, e^{-ih\frac{2\pi}{N_{div}}n_t} \tag{2.38}$$

in which h is the time harmonic index (or Engine Order), p_t is the discrete equally spaced pressure signal in time and N_{div} is the total number of samples. The resulting complex Fourier coefficients $P^{(h)}$ extracted on blade surfaces grid points are further

spatially decomposed along the circumferential direction to determine the rotating perturbation that will excite the corresponding traveling wave mode shape. The time-space Fourier coefficients are extracted along corresponding points on grid surface as follows:

$$\hat{P}_{(m)}^{(h)} = \frac{1}{NB} \sum_{k=1}^{NB} P_k^{(h)} \, e^{-im\frac{2\pi}{NB}k} \qquad (2.39)$$

in which m is the circumferential order, $P_k^{(h)}$ the discrete time Fourier coefficient tangential distribution on blade corresponding surface points and NB the blade count. The spatial decomposition is usually employed in aeroacoustics where this circumferential decomposition is performed along the computational grid, instead of along corresponding points on blade surface mesh as in the presented case, in the annular duct between rows to extract noise components in terms of their acoustic power. In the time-space decomposition, the circumferential DFT is thus performed on a coarse down-sampled set of only NB samples taken on each blade at corresponding positions (grid points) on the surface. Hence, the extracted rotating pressure components have a number of lobes ranging from $-NB/2$ to $+NB/2$ or from $-(NB-1)/2$ to $+(NB-1)/2$ in case of odd blade count as suggested by the Nyquist's theorem. It is clear how this approach also takes into account the aliasing phenomenon experienced by the blade-row when excited by a rotating perturbation with a lobe number higher then $NB/2$.
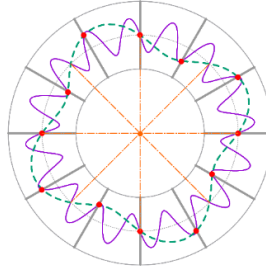
Figure 2.25: Sketch of lobe circumferential pattern and aliasing [**26**]

Figure 2.25 provides a visual representation of a possible excitation scenario, where a rotating perturbation with 16 lobes, represented by the solid violet line, impinges on a row composed by 12 blades represented by the radial grey segments. The 12 blades experience a 4-lobe perturbation represented by the green dashed-line due to the aliasing phenomenon. The orange dashdot radial lines highlight the resulting 4 nodal diameters associated to the 4-lobe excitation. The proposed spatial decomposition on "blade-sampled" corresponding NB points along the circumferential direction is thus able to convert the 16-lobe incoming perturbation into the 4-lobe excitation experienced by the blade-row which will finally vibrate as a traveling wave with 4 nodal diameters. Therefore, it is essential to evaluate all the possible rotating lobes that compose a single engine order perturbation: each spinning lobe can be seen as direct or aliased excitations for the blade-row. Tyler and Sofrin [27] theory states that rotor-stator interactions generate pressure spinning lobes, that are in fact acoustic waves, which travel along the machine causing additional "acoustic excitations" for a given blade row. The concept of Tyler and Sofrin modes is thus employed to decompose the overall perturbation, including also the propagations effects and further scattering by previous or successive

blade rows. The generalized stator-rotor interaction theory predicts the generation of rotating perturbations with the number of lobes m (i.e. the circumferential order) and angular frequency ω in the different frames of reference (fixed or rotating with rotational speed Ω). The pressure rotating lobes in the frame of reference of the rotor are characterized by:

$$m_2 = k_1 N_1 - k_2 N_2 \tag{2.40}$$

$$\omega_2 = k_1 N_1 (\Omega_1 - \Omega_2) \tag{2.41}$$

where N is the blade count and k is an integer value called harmonic or scattering index and Ω the rotational speed. Such acoustic perturbations travel upstream and downstream with different propagating behaviors depending on the axial wave number k_x. The k_x quantity can be real, the corresponding acoustic mode of which is cut-on, or complex with cut-off mode. Cut-off modes decay as they propagate axially, whereas cut-on waves keep their amplitude unchanged resulting more dangerous for aeromechanical and acoustic implications. Moreover, a single pressure perturbation also experiences successive scattering when propagating across successive blade rows. The scattering effect due to a further blade rows generates new sets of rotating perturbations with a circumferential order related to the fundamental propagating one. Scattered waves also change their angular frequency with respect to the fundamental one when analyzed in a different frame of reference where the scattering occurs. For instance, when studying spinning lobe frequencies in the absolute frame of reference (the statoric frame), stator scattering does not alter the fundamental frequency, while rotor scattering generates scattered perturbations with new frequen-

cies. Conversely, in the rotor frame of reference, the stator scattering produces additional rotating lobes with different frequencies [26]. Therefore, it is evident that the scattering phenomenon, due to the interaction of Tyler and Sofrin modes with successive blade row, generates several additional perturbations not immediately detectable and potentially dangerous for all the blade rows.

To sum up, the proposed unsteady forcing decomposition, based on time and space circumferential DFT, allows the decomposition of an overall pressure fluctuation, coming from unsteady simulations, in rotating pressure components (also accounting for aliasing phenomena) that can be individually applied to the corresponding travelling wave mode shape, in order to evaluate the forced response problem by means of the modal work approach or FRA analysis.

2.4.3 Modal work approach

The response of a mechanical system subjected to harmonics excitations can be evaluated by introducing the concept of modal work and modal force. This method is based on energetic considerations and the fundamental assumption is that the work done by the harmonic excitations is completely dissipated by the damping sources in the system. Under this assumption it is possible to compute a scaling factor that can be applied to modal displacements and stresses to obtain the actual displacement and oscillating stress. So, it is not necessary to make use of the damped full harmonic analysis. For the cyclic system like a blade-row, the modal work approach determines the maximum energy transfer of a rotating pressure perturbation, decomposed on blade corresponding points, and defined by the circumferential order, applied to the corresponding traveling wave mode shape defined by the nodal diameter. Given the fact that the

relative phase between the pressure distribution and the modal displacement is undetermined, the maximum value of the modal work is searched for by maximizing the expression for a generic phase.

For presenting the approach, let us consider the work per cycle produced by a sinusoidal force during a steady forced vibration. This work must be equal to the energy dissipated during one cycle by the damping force as follows:

$$\pi dF \sin\alpha = \pi\zeta d^2\omega \tag{2.42}$$

where α is the phase between force and displacement, d are the displacements, F is the modal force, ω is the angular frequency, and ζ is the actual damping. It may be assumed with sufficient accuracy that this amplitude occurs at resonance condition where $\alpha = \pi/2$, and so:

$$\pi dF = \pi\zeta d^2\omega = 2\pi\xi d^2\omega^2 \tag{2.43}$$

from which

$$d = \frac{\pi dF}{2\pi\xi d\omega^2} = \frac{F}{2\xi\omega^2} \tag{2.44}$$

Same conclusion can be drawn for a distributed forcing acting on component modal displacements and leading to the modal force concept. In reference to the above formulae, it can be demonstrated that the scaling factor for the displacements d,

and for the stresses, depends on modal force F_m, the aerodynamic damping ξ and the square of angular frequency ω as summarized in the following formula:

$$d = \frac{F_m}{j2\xi\omega^2} \qquad (2.45)$$

where j is the imaginary unit. Finally, the modal force can be computed by the complex dot product between the conjugate of the modal displacement δ_m^* coming from modal analysis in cyclic symmetry and the aerodynamic forcing F_a spatially decomposed to match the nodal diameter of the mode shape as follows:

$$F_m = \sqrt{\left[\iint_\Sigma \Im[\delta_m^* F_a]\, d\Sigma\right]^2 + \left[\iint_\Sigma \Re[\delta_m^* F_a]\, d\Sigma\right]^2} \qquad (2.46)$$

2.4.4   HCF life assessment

Once evaluated the forced response amplitudes and calculating the oscillating stress distributions, high cycle fatigue assessment can be carried out. In particular, stress distribution is identified using strain gauges placed in various positions on the blade to measure blade strains for each natural mode. The Goodman diagram is usually adopted to evaluate response amplitude and the allowable static and alternating stresses of the blade [28] [29]. This diagram can be built starting from the ultimate and fatigue strengths of material properties, experimentally evaluated through tests at different temperatures. Once that the ultimate strength at zero vibratory stress and the fatigue strength at 10^7 (or more) cycles are measured, a straight line can be drawn between these two values to define the infinite life area.

Notch factor, standard deviation of measured data, and temperature are the main parameters which can affect the distribution of mean fatigue strength and, thus allowable alternating stress [22]. The fatigue notch factor is related to a stress concentration factor which is a ratio of the maximum steady stress to the unnotched steady stress of a particular geometry such as notches, fillets, holes, etc. The standard deviation factor, which is obtained from test data, accounts for variations in the fatigue strength due to composition changes of the material and processing differences between components. A minus three sigma (-3σ) value of fatigue strength accounts for 99.865% of all pieces having a fatigue strength greater than this value. The temperature affects both the ultimate and fatigue strengths and subsequently an increase of temperature reduces the resistance of the material. Goodman diagram is thus modified using the notch factor and finally considering a "safety" coefficient which takes into account the -3σ value of fatigue strength. It can be concluded that infinite life of the blade is ensured if both steady and alternating stresses stay below the line, as shown in Figure 2.26.
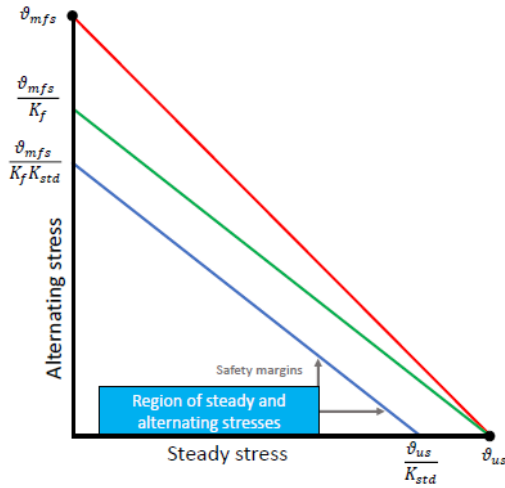
Figure 2.26: High Cycle Fatigue assessment

2.4.5 Design flutter-free

Flutter is defined as a self-excited and self-sustained aeroelastic instability that involves vibration of a structure when exposed to a fluid flow. The flutter phenomenon belongs to the family of asynchronous vibration problems, thereby meaning that flutter is not caused by the interaction between upstream and downstream blade rows. The difference between flutter and resonant vibrations in turbomachines is that the flow unsteadiness leading to structural oscillation is induced by the motion of the structure itself rather than external sources. In fact, from a physical point of view, flutter occurs when the blade is absorbing energy from the flow instead of from unsteady external forces. The vibration starts with small amplitudes and then exponentially increases by the energy exchange with the fluid flow, thus reducing the fatigue life and leading to structural failure.

2. Fundamentals of Axial Turbine Aerodynamics and Aeromechanics

In turbomachinery, flutter usually appears in the fore part of compressors or in the aft part of turbines, where blades have high aspect ratio and high loads as:

- Fan

- Low pressure gas and steam turbines blades

- Low pressure compressor stages

Flutter in compressors has been more extensively studied than flutter in turbines, however the same map as for compressor can be drawn. Figure 2.27 shows the characteristic line of a turbine with the different type of flutter regions.
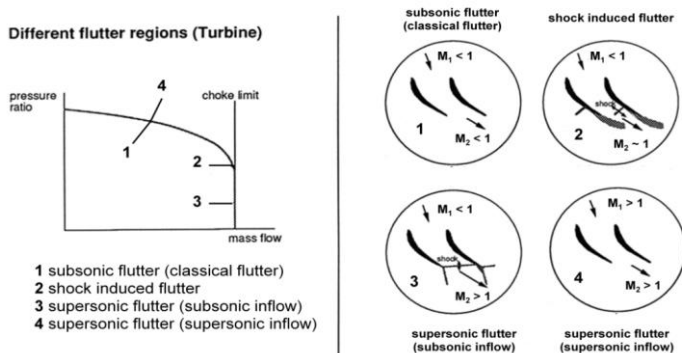
Figure 2.27: Flutter map for turbines [30]

As in compressors, four main categories of flutter can be encountered: classical flutter, shock induced flutter, supersonic flutter with subsonic inflow, and supersonic flutter with supersonic inflow.

1. Classical flutter. This flutter can occur when the flow is attached to the blade with no separation and a phase lag between the aerodynamic forces and the amplitudes

of vibration exists. Three possible situations can be presented: (1) the flow introduces energy in a not damped structure producing uncontrolled oscillations (unstable condition); (2) the flow absorbs energy from the structure, and this produces an always stable operative condition; (3) the energy introduced by the flow is balance by the dissipative energy of the structure producing Limit Cycle Oscillations (LCO).

2. Shocked induced flutter. When in the throat region the sonic Mach number is reached, the turbine is chocked, i.e. mass flow across the turbine can no longer increases and all the curves collapse. The sonic blockage in the stator generates a shock which may induce flutter.

3. Supersonic flutter with subsonic inflow. This type of flutter can be generated by an oblique shock wave which occurs downstream the throat section.

4. Supersonic flutter with supersonic inflow. Similar to classical flutter, this type occurs with supersonic Mach numbers.

This aeroelastic interactions occurring inside a turbomachinery are thus a complex phenomenon that should be analyzed and prevented. During a flutter design procedure is necessary to keep under control numerous flow and structural parameters. In fact, unlike the forced response design, where resonance conditions may be predicted with simple tools as Campbell or ZZENF diagram previously described, flutter design requires dedicated CFD analyses [31] and experimental campaigns. Generally, a good flutter design aims to develop blade geometries with safety flutter margins for all the operating range. As explained by Srinivasan [32], although numerous parameters influence the

aeroelastic behavior of a bladed disk, only some of them and some specific features are considered crucial.

- **Reduced frequency**

  This parameter is defined as the ratio of the time taken by the fluid to pass through the blade chord to the blade oscillation period. In formula, this corresponds to:

$$k = \frac{b\omega}{V} \tag{2.47}$$

  where b is the semi-chord, ω is the frequency of vibration in radians/sec, and V is the inlet or outlet relative velocity. Another equivalent interpretation of the reduced frequency is also given in the literature and relate the chord to the wavelength drawn downstream by a sinusoidal oscillation (see Figure 2.28).

$$k = \frac{b}{\lambda} \quad where \quad \lambda = \frac{u}{\omega} \tag{2.48}$$
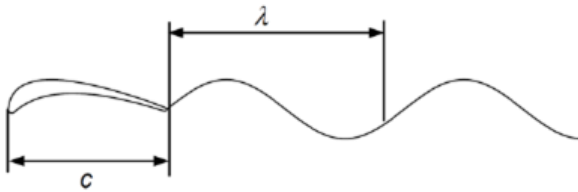
Figure 2.28: Graphical interpretation of reduced frequency [33]

  So, low reduced frequency means that the shed vortices have travelled a distance longer than the chord, so these

vortices do not interact with the blade, and the flow is likely to be steady. For large values of reduced frequency, unsteady effects become dominant causing instabilities. For turbomachine blade, critical reduced frequencies have been reported in the range between 0.1 and 1.0.

- **Mass ratio**

  The mass ratio (μ) is the ratio between the solid body mass and the mass of a representative fluid volume surrounded in a defined circle. The parameter is calculated as:

$$\mu = \frac{4m}{\pi\rho b^2} \tag{2.49}$$

In the expression, m is the solid mass per unit blade span, ρ the flow density per unit blade span and b is the airfoil semi-chord length that is equal to the circle radius used to define the fluid mass. Figure 2.29 illustrates the concept of mass ratio μ.
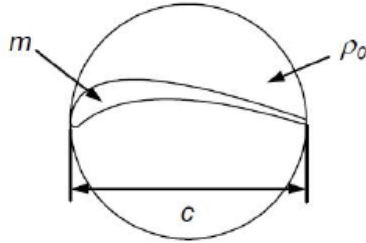
Figure 2.29: Mass ratio [33]

Decreasing values of mass ratio indicate increasing flutter onset risk.

- **Mach number**

  This parameter describes the nature of the unsteady flow field whether it be subsonic, transonic or supersonic. Likewise, the reduced velocity, high values of Mach are related to flutter instability conditions.

- **Blade loading parameter**

  Incidence, pressure ratio, diffusion factor and, margin to choke are parameters which have been used to describe the blade loading. They can have an impact on flutter stability.

- **Pressure and density**

  The primary effect of changing density or static pressure is a proportional variation in unsteady aerodynamic work per cycle and therefore in aerodynamic damping. Increasing the gas density is stabilizing if aerodynamic damping is positive. Likewise, increasing the gas density is destabilizing if aerodynamic damping is negative.

- **Mode shapes**

  The unsteady aerodynamic work is a function of the vibratory mode shape because the modal characteristics affect vibration frequency, amplitude, and shape. The phase between unsteady pressure due to blade displacement and the blade displacement itself determines whether the flow is feeding energy to the blade or vice versa.

Flutter stability is influenced both by the aerodynamic parameters and the blade dynamic behavior. Flutter design strategy is based on three steps. The first step aims to perform the aerodynamic design of the blade with a steady state CFD analyses

and to obtain the aerodynamic parameters which will impact on aerodynamic damping evaluation. By conducting a modal analysis, the modal displacement and mode shapes of the system are determined. Finally, a flutter analysis is performed combining the steady state aerodynamics and dynamics results.

In the uncoupled methods, the aeroelastic stability is assessed by evaluating the sign of the aerodynamic work, which is obtained as the unsteady pressure integration overall the blade surface within a single oscillation period:

$$W_{aero} = \int_{t}^{t+T} \int_{S} (-p)\vec{n} \cdot \vec{c}_{blade} \, d\Sigma \, dt \qquad (2.50)$$

where p is the pressure field over the blade, $\vec{n}$ is the surface outgoing normal vector, $\vec{c}_{blade}$ is the velocity field over the blade, Σ is the blade surface and T is the vibration period. The direction of net exchange is the criterion for aerodynamic stability: globally, the aerodynamic work per cycle (W_{aero}) describes the work exerted by the fluid on a given blade during one period of its motion. In this context a positive work entry ($W_{aero} > 0$) indicates that energy is transferred from the air flow to the structure, leading to destabilizing unsteadiness. On the contrary, for a negative work entry ($W_{aero} < 0$), the blade releases energy so that the blade itself is damped. Therefore, for a stable motion, the integer of the aerodynamic work must be negative.

In order to check flutter stability, also the overall damping of the system can be checked. The total damping $\delta_{overall}$ is defined as the sum of the aerodynamic and structural damping:

$$\delta_{overall} = \delta_{structural} + \delta_{aero} \qquad (2.51)$$

and when $\delta_{overall}$ is negative, the system is unstable. Nevertheless, the mechanical damping is always positive, therefore the only contribution to instability comes from a negative value of aerodynamic damping δ_{aero}. The aerodynamic damping, also called critical damping ratio (or energetic damping) ξ, is derived from the aerodynamic work normalization, as shown in the following formula:

$$\xi_{aero} = \frac{-W_{aero}}{8\pi E_{kin}} = \frac{-W_{aero}}{2\pi m\omega^2 a^2} \qquad (2.52)$$

where E_{kin} is the blade average kinetic energy, m is the blade modal mass, a is the modal amplitude and, ω is the angular frequency. So, once any random excitation causes a small vibration of the blade, three different scenarios might occur (see Figure 2.30).
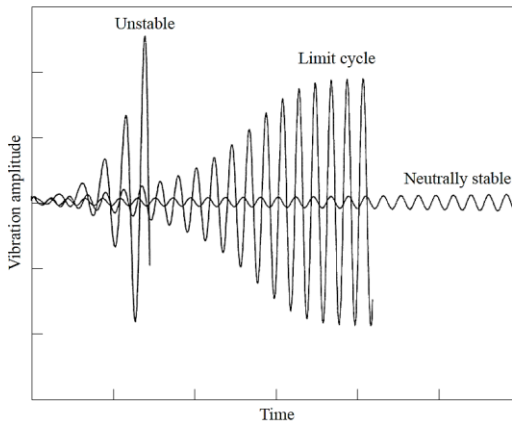
Figure 2.30: Possible scenarios of blade row vibration [31]

If the critical damping ratio is positive, the blade vibrations are always damped. When the overall damping is equal to zero, the

mode is considered marginally stable, which means that the oscillation amplitude remains constant. In the worst condition, when critical damping ratio is negative, the blade absorbs energy from the flow. If the energy absorbed is greater than that dissipated by the structural damping, the blade vibratory amplitude is amplified over time. Since structural damping is low and often negligible as already mentioned, the principal flutter stability criterion is to have a positive critical damping ratio values for all the nodal diameters. An example of the aerodynamic damping curve is reported in Figure 2.31.
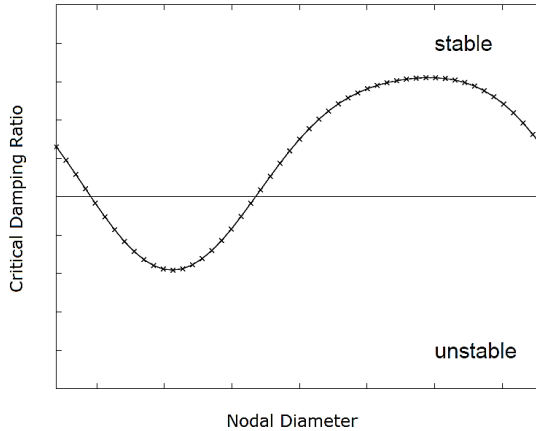
Figure 2.31: Stability curve

3 Numerical Methods

In this chapter, an overview of the CFD solver employed for the numerical simulations, the TRAF code, developed by the research group led by Prof. Andrea Arnone, is presented. Once introduced the key aspects of the solver, which is used for both steady and unsteady analysis, the focus will be on the numerical aeroelastic methods, both coupled and uncoupled, for flutter assessment. Then, a brief description of dedicated periodicity conditions for flutter computations is provided: full annulus and phase-lagged approaches used to impose the circumferential boundary conditions are explained.

3.1 TRAF code

All the numerical computations carried out within this work has been performed with the CFD code called TRAF (TRAnsonic Flow), developed by the research group of the Department of Industrial Engineering of the University of Florence led by Prof. Arnone. The code is a 3D URANS viscous and inviscid flow solver, designed for cascade internal flow predictions and includes several techniques to achieve computational efficiency and accuracy based on the solution of Reynolds averaged Navier-Stokes (RANS/URANS) equations written in conservative form and mapped in a curvilinear coordinate system. The link between the Cartesian coordinate system and the curvilinear one is handled by means of transformation matrices and Jacobian. [34] [35].

Several turbulence closures have been implemented in the TRAF code, ranging from algebraic to more complex one- and

two-equation models. A complete list of the turbulence models available is the following:

- Baldwin-Lomax algebraic model [36]

- Degani-Schiff algebraic model [37]

- Mixing length algebraic model [38]

- One-equation Spalart-Allmaras model [39]

- One-equation Spalart-Allmaras model with Spalart-Shur correction [40]

- Two-equation k-ω Wilcox Low-Reynolds model [41]

- Two-equation k-ω Wilcox High-Reynolds [42]

- Two-equation k-ω Menter SST model [43]

As far as the spatial discretization is concerned, the code is based on a finite-volume approach, with the governing equations discretized in space starting from an integral formulation and without any intermediate mapping [44]. The viscous terms are discretized using 2nd order accurate central differences, while for the inviscid fluxes a 2nd order cell-centered scheme or a Roe's+TVD (upwind scheme) may be employed. If the cell-centered scheme is adopted, the fluxes are computed by a simple averaging of adjacent cell-center values. To assure stability and prevent oscillations near shocks or stagnation points, artificial dissipation terms are also included away from the shear layer regions, where the physical diffusion associated with diffusive terms is generally not sufficient to prevent the possible odd-even point decoupling typical of centered schemes. Both scalar [45] and matrix [46] dissipation models are available in the code. For

artificial diffusion minimization inside the shear layers, an eigenvalue scaling technique is adopted [47]. As far as the upwind scheme is concerned [48], a higher order of spatial accuracy is achieved through a MUSCL (Monotone Upstream-centered Schemes for Conservation Laws) extrapolation scheme (3rd order spatial discretization). To avoid numerical instabilities, a TVD (Total Variation Diminishing) scheme is applied [49].

To compute the time varying solution, the code utilizes a time-marching method with dual time stepping approach. Some different techniques to speed up the convergence and reduce the computational cost are used [50]:

- Local time-stepping

- Residual smoothing

- Multigrid

- Grid refinement

The first method is often applied when dealing with time-marching approach since a faster expulsion of disturbances can be attained by locally using the maximum available time step. The local time step limit is computed accounting for both the convective (Δt_c) and diffusive (Δt_d) contributions:

$$\Delta t = CFL\left(\frac{\Delta t_c \Delta t_d}{\Delta t_c + \Delta t_d}\right) \qquad (3.1)$$

where *CFL* is the Courant-Friedrichs-Lewy number.

The idea of multigrid is based on obtaining coarse meshes by simply eliminating mesh lines in each coordinate direction from the finer reference mesh, thus leading to a convergence speed

up. The procedure is repeated on a succession of coarser grids and the corrections computed on each coarse grid are transferred back to the finer one by bilinear interpolations. Even if more grid levels may be adopted, usually the multigrid method is performed with a V-cycle on three grid levels: coarse (4h), medium (2h) and fine (h) [51]. The Full Multigrid approach is obtained with a grid refinement strategy at the beginning of the simulation, used to provide a cost-effective initialization of the fine grid solution: the solution provides a cost-effective initialization of the fine grid solution; then, the solution is moved by bilinear interpolations to the finer grid and this procedure is repeated as long as the finest grid level is not reached [52]. The convergence evaluation is based on the residual check, defined as:

$$Q = \frac{1}{N} \sum_{n=1}^{N} (\sum_{i=1}^{5} Q_i^2)^{1/2} \qquad (3.2)$$

where $N = nx \cdot ny \cdot nz$ are mesh cells and the target for convergence is half-order above the machine accuracy (single precision).

In turbomachinery configurations there are five main types of boundary conditions: inlet, outlet, solid walls, periodicity, and interface between adjacent rows. The radial distributions of total temperature, total pressure and flow angles are prescribed at the computational domain inlet, while a spanwise distribution of static pressure, or a value at the casing used to impose a radial equilibrium, is required at the domain outlet. On the solid walls within the computational domain, no-slip and temperature conditions are used to compute the values for density and total energy. The periodicity in circumferential direction is imposed by setting periodic phantom cell values as a phantom-cell layer

is present for each grid boundary. Linear interpolations are performed in order to set a reasonable value for the dependent variables in phantom cells in case of grid lines do not match at the periodicity interface. Despite the fact that this approach cannot guarantee a complete conservation of mass, momentum and energy, in most of the applications no accuracy losses have been experienced, if no strong gradients occur along non-periodic grid boundaries with high differences in cell sizes. As far as boundary conditions for the interfaces between adjacent rows are concerned, a different treatment is adopted for the time-accurate and the steady state case. When running an unsteady analysis, the coupling between consecutive rows is handled by means of sliding interface planes, with the exchange of information between adjacent blocks obtained performing linear interpolations in both the tangential and the radial direction [53]. Differently, for steady simulations, mixing planes with non-reflecting capability are used to handle the coupling between adjacent rows. Data exchange through the common interface plane of consecutive rows is obtained by an appropriate calculation of phantom cell values, keeping the spanwise distribution while averaging in the pitch-wise direction.

In order to properly exploit the computational power available nowadays, the TRAF code provides a multi-level hybrid strategy for parallelization on CPUs [54]. This hybrid scheme is obtained from the coupling of OpenMP and MPI parallelism.

For aeroelastic analysis, the TRAF solver employs an uncoupled method, computing the aerodynamic work and hence the critical damping ratio, as explained in paragraph 2.4.5. The CFD code is also capable to solve both tuned and mistuned blade-row.

3.2   Aeroelastic methods overview

A very wide range of CFD methods have been developed since the first appearance of digital computers. The increase in computing power during recent years and advances in computational fluid dynamic methods have allowed to obtain detailed assessment of unsteady aerodynamic flow field for multi-row domains. Nowadays, aeroelastic analyses are mainly carried out with numerical techniques in the context of the Computational Aeroelasticity (CA). This branch investigates the aeroelastic interaction issues of structures.

For forced response analysis, unsteady simulations based on URANS non-linear method with difference level of accuracy are now usually employed, while for flutter assessment different unsteady formulation have been developed. The interaction between flow and moving bodies is usually simulated by numerical solvers thus providing a design tool that may be applied, for example, to assess if a blade in a certain operating condition is stable or not. Marshall and Imregun [31] give a review of a wide range of possible approaches, highlighting advantages and limitations. Among these, three modeling methods may be employed for the numerical Navier-Stokes equations solution of the flow around moving bodies:

- Time-linearized method

- Non-linear harmonic method

- Non-linear method

Although various models have been developed to computationally assess flutter occurrence, there are mainly two macro-categories, distinguished in relation to the way in which interactions between flow and solid body are resolved:

- Uncoupled method

- Coupled method

3.2.1 Uncoupled method

Uncoupled methods are based on the separate integration of dynamic motion equations to compute solid body structural behavior and, Navier-Stokes equations for flow field evaluation. This approach allows the aerodynamic calculations to be performed independently to the blade dynamics, offering considerable savings in computing requirements. In an uncoupled aeroelastic approach (see Figure 3.1), blade mode shapes and natural frequencies are provided by a modal analysis on the Computational Solid Domain (CSD). At the same time, the average pressure field on the blade surface has calculated with steady state analysis solving iteratively the Navier-Stokes equations. Then, the mode shapes are transferred from solid to fluid domain and a harmonic deformation is applied to the CFD mesh to evaluate the unsteady response around the oscillating blade-row. The solver is able to evaluate the unsteady pressure response over the blade surface, while the blade row vibrates in a travelling wave manner with a constant phase shift between adjacent blade passages and with the same amplitude and frequency.
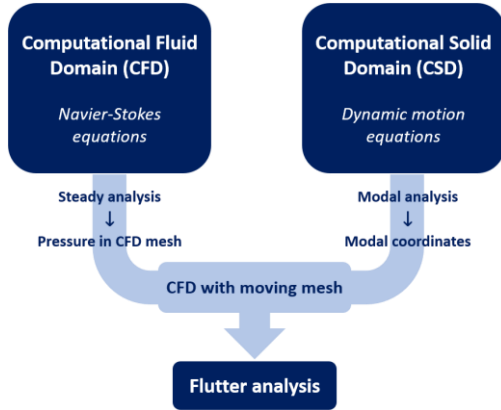
Figure 3.1: Uncoupled method scheme

Traditionally, the uncoupled method has been used for flutter prediction and has been extended to forced response calculations to obtain the aerodynamic damping in more recent years. Flutter calculations are concerned with determining the aeroelastic stability of the system, indicated by the direction of energy flow resulting from the blade vibrating in the fluid.

In this work, the aeroelastic computations has been performed with TRAF code, which is an URANS CFD solver as previously explained in 3.1. The unsteady equations are solved in time on the deforming mesh using a dual time-stepping technique until the flow solution becomes periodic. Since TRAF employs an uncoupled method, blade vibrations are assigned with a constant amplitude: consequently, flutter stability cannot be assessed by looking at the evolution of the oscillation amplitudes, because blade oscillation is kept constant. To assess flutter stability, the critical damping ratio is calculated from the aerodynamic work, as indicated by the Energy Method. This method proposed by Carta [55] calculates the net energy transfer between a vibrating body and the flow induced pressures of the surrounding fluid

during a period of blade oscillation. The energy method is based on the assumption that the effects of the aerodynamic forces on the structural dynamics properties are negligible, so the unsteady aerodynamic blade loading does not affect natural frequencies and mode shapes. This assumption is verified if a significant frequency gap between different eigenmode families is present and the mass ratio parameter of the vibrating system is high.

The aerodynamic work, shown in Eq. (2.50) is computed by the numerically integration of the unsteady pressure over the blade surface and over time. Therefore, if the work is positive, the energy transfer is from the flow to the blade. Otherwise, a negative work indicates that the blade dissipates its energy, and the oscillations are damped.

3.2.2 Coupled method

Coupled methods solve simultaneously fluid and solid domain computations taking into account the bi-directional interaction between blade vibration and flow field. Fluid unsteadiness changes blade dynamics in terms of vibration frequencies and amplitudes, with the consequence that blade movement has no more constant magnitude, pulsation and inter blade phase angle. The frequency of the oscillation will also be shifted from the structural eigenfrequency of the system, especially when the mass ratio is small. For this method, the system of equations that have to be solved, are represented by:

$$\underline{M}\,\underline{\ddot{x}} + \underline{C}\,\underline{\dot{x}} + \underline{K}\,\underline{x} = \underline{F}_{ext}(t) \tag{3.3}$$

$$\frac{\partial \underline{U}(t)}{\partial t} + \underline{\nabla} \cdot \underline{\Phi} = \underline{Q} \tag{3.4}$$

where Eq. (3.3) represents the dynamic equations governing structural vibration of the blade already mentioned in paragraph 2.4; Eq. (3.4) represents the Navier-Stokes equations in the divergence form, where $\underline{U}$ includes the conservative variables for mass, momentum, energy and for turbulence quantities, $\underline{V}$ incorporates the three flux functions and $\underline{Q}$ is the source term column. The equations are simultaneously integrated in time so that the fluid and structural domain are coupled exchanging boundary conditions, as shown in Figure 3.2.
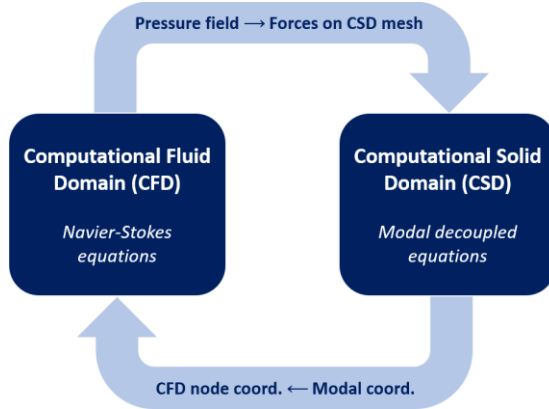
Figure 3.2: Coupled method scheme

A CFD solver integrates the unsteady Navier-Stokes equations in time domain on the deforming mesh. The unsteady static pressure field on the blade is transferred from the CFD grid to the CSD grid and the corresponding modal forces are then computed. The computational effort is decreased by reducing the structural equations to a small number of orthogonal modal equations which can be integrated in time. Node displacements are transferred from the CSD mesh to the CFD mesh determining the CFD mesh deformation. All these operations are iterated for each discrete physical time-step.

In fully coupled approaches, the level of interaction between the fluid and structural domains can vary from partially integrated schemes to fully integrated schemes. In the partially integrated schemes, the equations governing the problem are resolved separately by exchanging information on the interface between the fluid and the solid at each time step. Fully integrated methods combine the fluid and structural equations into a single numerical integrations scheme, solving the entire system without the need to transfer information between meshes at each time steps. Flutter stability is assessed by looking at the evolution in time of the amplitude of the various traveling waves and not computing the aerodynamic work.

3.2.3 Periodicity conditions in time

For flutter analysis periodicity conditions are a key aspect to reduce the computational requirements. Several approaches are available in TRAF to impose circumferential periodicity conditions. Two different approaches are briefly described in the following focusing on uncoupled non-linear flutter simulation to correctly reproduce travelling waves:

- Full annulus approach

- Phase-lagged approach

3.2.3.1   *Full annulus approach*

The *full anulus* approach consists in simulating the entire annular row to reproduce all the possible travelling waves deformations with different IBPAs in order to evaluate the unsteady pressure response over vibrating row blade surfaces. This approach requires a wide availability of computational resources since the entire annulus must be simulated. The computational domain can be reduced simulating the sufficient number of

blades to reach the circumferential periodicity. The minimum number of vanes required to ensure instantaneous circumferential periodicity depends on IBPA of the studied sector, as explained in Eq. (3.5):

$$n_{passages} = \frac{2\pi}{|IBPA|} z \quad with \ z \in \mathbb{Z} : z > 0 \quad (3.5)$$

where z is an integer number which provides the periodicity of the investigated passage inside the row. Except for the IBPA=0°, the other values of IBPA need more than one vane to impose instantaneous periodicity condition; for example, IBPA=90° needs 4 passages as shown in Figure 3.3, while IBPA=72° requires 5 blocks, and so on. When $n_{passages}$ is equal to z, the computations must be performed on the whole cascade, determining high computational cost. This happens, for example, when a prime number of blades is present in a row. In this work, the full annulus approach has been adopted to evaluate the rotor-stator unsteady interaction due to the downstream wakes on a LP turbine rotor, discussed in the following.
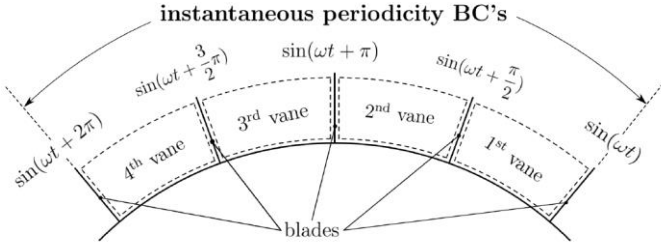
Figure 3.3: Instantaneous periodicity condition for a *full annulus* approach with IBPA=90°

3.2.3.2   *Phase-lagged approach*

The *phase-lagged* formulation imposes chorochronic periodicity conditions of Gerolymos [56] on circumferential boundaries for allowing to perform simulations at any IBPA, utilizing a reduced computational fluid domain. The computation of a single passage per row is sufficient to rebuild the unsteady flow solution of a row for each possible travelling wave, providing identical results to the full annulus approach. With the aim to enhance the convergence to a periodic solution, two passages per row are computed (Figure 3.4), making the approach more robust and quicker [57].
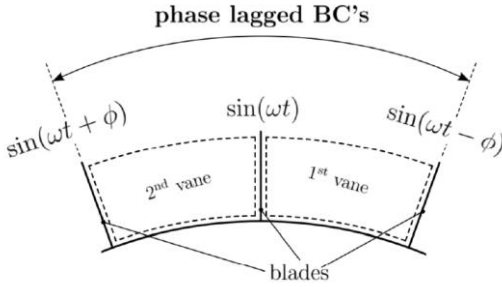
Figure 3.4: Periodicity conditions for a *phase-lagged* approach with a general IBPA value

Since the simulations are unsteady, each quantity directly depends on time, so that a generic solution variable at a periodic boundary $f(t)$ is expressed by Fourier series in time with a finite number of time-harmonic coefficients as below:

$$A_0 = \frac{1}{T} \sum_{j=1}^{NP} f(t) \Delta t \tag{3.6}$$

$$A_n = \frac{\omega}{2\pi} \sum_{j=1}^{NP} f(t) \sin(n\omega t) \, \Delta t \qquad (3.7)$$

$$B_n = \frac{\omega}{2\pi} \sum_{j=1}^{NP} f(t) \cos(n\omega t) \, \Delta t \qquad (3.8)$$

where A_0, A_n, B_n are the Fourier series constants, n the harmonic number, ω the natural pulsation, T the blade oscillation period, NP time-step number on the oscillation period and Δt is the Fourier series constant amplitude in time. A_0, A_n, B_n constants are stored in memory for a prearranged harmonic number and are used to recontract fluid properties through a suitable phase lag, linked to the IBPA in case of aeroelastic analysis. To accelerate the convergence, the formulation implemented in the TRAF code updated the coefficients even during the period of oscillation through a moving average scheme.

4 Numerical Procedure for Axial Turbine Analysis

This chapter describes the numerical setup used within this work. Firstly, the main steps of the workflow are illustrated. The CFD calculations outputs, representing the aerodynamic design phase, are combined with the modal and structural analysis outputs to calculate the system forced response. Starting from the fluid domain discretization, particular attention is given to steady and unsteady computations, from mesh creation with an in-house tool, to the analysis setup. Indeed, the harmonic content of the aerodynamic force is obtained by evaluating the blade unsteady pressure distribution obtained by URANS simulations. The two operative points investigated are also presented and discussed. Finally, the mode shapes transfer process from solid to fluid domain grid is described to impose the frequencies and mode shapes calculated on the solid domain surface to the blade grid boundaries of the flow domain, for the non-linear uncoupled flutter computations with moving grid.

4.1 Workflow overview

The design procedure gives an idea of the interrelationship between thermodynamic, aerodynamic, mechanical and control system design. Considering the aeromechanical field, several procedures have been recently developed to achieve a safe blade row design [58] [59] [60] . All these methods are based on structural dynamic solvers and aerodynamic codes to evaluate components dynamic and to compute the fluid flow unsteady response caused by blade vibrations, respectively. In this context a numerical procedure to integrate the aerodynamic design

phase with the aeromechanical one has been drawn up. The workflow scheme, which shows the steps and the connections of the aeromechanical procedure, is reported in Figure 4.1.
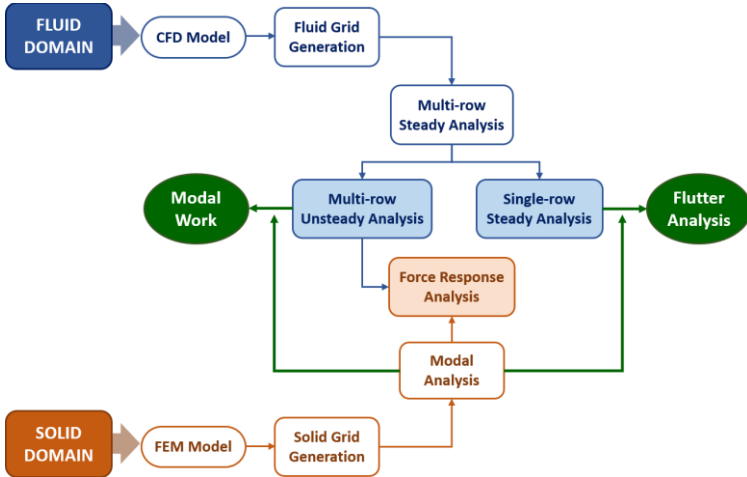
Figure 4.1: Procedure scheme

The first step concerns the discretization of the fluid domain. Starting from the CAD model, a structured grid has been generated using an in-house tool to perform a multi-row steady state analysis by means of the TRAF code. This solution is used to initialize the following unsteady calculations from which the unsteady pressure distribution on blade surface is extracted. On the other hand, once the solid domain is discretized, a modal analysis is performed in parallel using the commercial code AN-SYS. The structure mode shapes, and natural frequencies obtained are employed as boundary conditions for the unsteady flutter analysis with vibrating blades and for the final modal work calculation. So, modal displacements are transferred from grid surface nodes from the solid domain to the fluid domain. Considering that the FEM and CFD blade surfaces are not in

the same position, an automatic method to find out the roto-translation matrix to overlap the two different domains is integrated in the tool-chain. Once the mode shapes are transferred, it is possible to carry out flutter analysis which allows the assessment of blade row stability and also to provide the overall damping as a function of the nodal diameter. For forced response analysis the same transfer strategy from FEM to CFD domain is used to interpolate the mode shape on the CFD grid surface where the harmonics of unsteady pressure distribution is extracted from multi-row unsteady analysis. These forcing functions are directly computed by a run-time DFT algorithm activated once the unsteady multi-row solution is periodic. The procedure is finally closed with the blade row HCF life evaluation of the final geometry by means of the Goodman diagram, where steady and alternate stresses, evaluated on each solid domain node, are compared with the material fatigue limit.

The all analysis in the fluid domain, including the final flutter evaluation and the modal work calculation, are the main objective of this activity. For this reason, the modal and structural analysis, reported in the scheme above, will not be further discussed in this work.

4.2 Industrial test case

The test case selected to apply the aeromechanical procedure for the forced response is a typical configuration of a light industrial gas turbine of Baker Hughes family for mechanical drive and power generation applications (Figure 4.2). This configuration, generally called 1.5 shaft engine, is composed by the High Pressure Turbine (HPT) module, aerodynamically coupled with the Low Pressure Turbine (LPT). A stationary component called Turbine Center Frame (TCF) connects the HPT to the

LPT module. The HPT drives the axial compressor in the gas generator, while the LPT runs connected to an independent shaft and drives a process compressor or a generator.
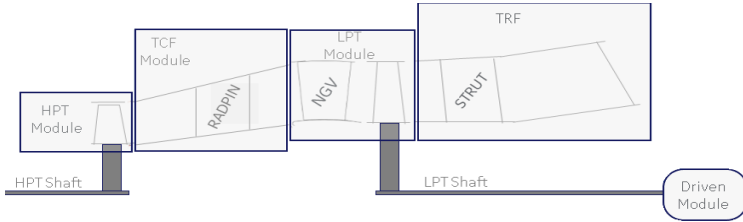
Figure 4.2: Turbine layout for a typical 1.5 shaft heavy-duty engine

The HPT and LPT modules have two stages each, labelled Stage 1 and Stage 2, and Stage 3 and Stage 4, respectively. The first stage of LPT is provided with moveable Nozzle Guide Vanes (NGVs), and discharges to the exhaust diffuser through the downstream Turbine Rear Frame (TRF) module. In this activity, the focus is on the LPT module and, in particular on the Stage 3 rotor row. A forced response analysis together with flutter stability assessment has been performed since a crossing within the operative range has been detected during the test campaign. During the first prototype run of the machine, in fact, aerodynamic and aeromechanic instrumentations have been installed. In Figure 4.3, the turbine machine sections where physical quantities are acquired, are presented.
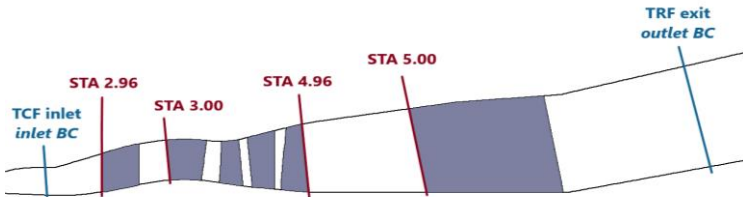
Figure 4.3: Machine test section with aerodynamic instrumentations

Measurements include static pressures (p) on hub and tip end-walls, total pressure (p_t) and total temperature (T_t) probes mounted at different span locations on the TCF leading edge, and on the TRF leading edge. The exhaust plenum flange is equipped with a measurement grid composed by twenty-one equally spaced probes for p_t, p_s and T_t across the discharge rectangular flange. Experimental data at the TCF module inlet, and downstream of the TRF module, are used as boundary conditions for the CFD analyses. The final part of the diffuser is not completely included into the computational domain, as it is deemed not strictly necessary for the purpose of the present work. Moreover, in this way it was possible to reduce the computational effort. Concerning the aeromechanical measurements, four strain gages have been installed on four blades of the LPT rotor row (B3) that is under investigation in the present work, Figure 4.4.
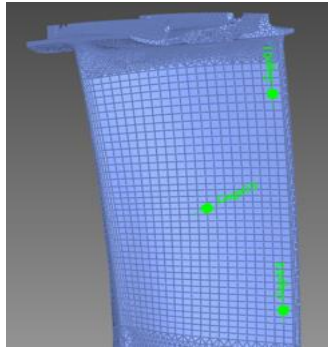
Figure 4.4: Positions of the four strain gage applied on four rotor blades (B3)

Further, different rotor shaft speeds have been investigated during the test. From a numerical point of view, two operating conditions have been considered: the full speed-full load (100%)

condition, corresponding at design point and the full speed-partial load (50%) condition, corresponding to an off-design condition (Table 4.1).

OP	Shaft Speed	Load
	$[rpm]$	$[-]$
OP1	7800.28	100%
OP2	7800.28	50%

Table 4.1: Aerodynamic operating points

4.3   Fluid domain discretization

The first important step of any CFD analysis is the discretization of computational fluid domain. The in-house mesh generator is able to realize two different mesh topologies. The designer may choose in advance between H- or O-type grid topologies, depending on the case study under investigation. For standard viscous Navier-Stokes simulations, the grid spacing near the wall is chosen to obtain a $y^+ \leq 1$ for the first grid from the wall. This condition allows a proper resolution of the boundary layer over solid walls.
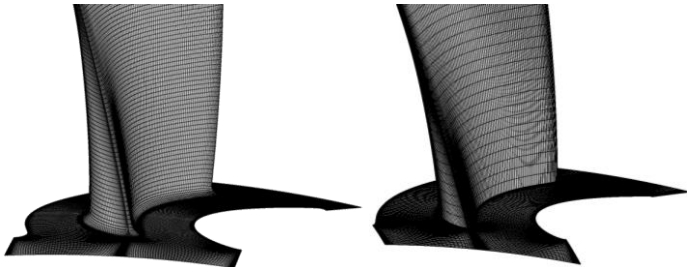
Figure 4.5: Viscous Full Navier-Stokes (left) and inviscid endwall (right) grids

It is worth highlighting that inviscid endwalls approach can be adopted where applicable (e.g. negligible diffusive fluxes in spanwise direction) in order to considerably reduce the computational cost of CFD analyses by removing the grid re-clustering which means very high points density near the endwalls.

4.3.1 Steady analysis

Steady-state analyses have been performed on the domain previously described at paragraph 4.2, from the inlet to outlet boundaries shown in Figure 4.3 respectively. A fully 3D H-type structured grid has been used with a y^+ value lower than 1 to discretize the blades passages for steady computations. Both the viscous and inviscid endwall formulations have been tested. Each block has typical dimensions of 157x81x25 grid points in streamwise, pitchwise, and spanwise directions, for inviscid endwall, respectively, while dimensions of 157x81x81 for the viscous approach. Therefore, the number of nodes for each vane is around 0.33 million for inviscid endwall formulation and around of 1.03 million for viscous one, respectively. A blade-to-blade section at midspan of the Full Navier-Stokes computational mesh of the two stages, Stage 3 and Stage 4, is reported in Figure 4.6.
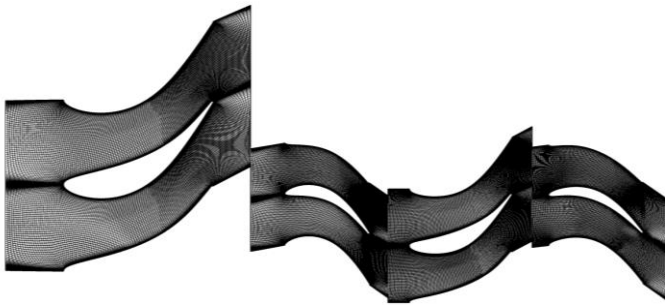
Figure 4.6: Blade to blade view of Stage 3 and Stage4 Full Navier-Stokes computational grid

Steady computations have been performed in order to evaluate the flow field characteristics and to select the numerical framework to be adopted for unsteady calculations. RANS analyses have been performed by using TRAF code described in Chapter 3 by imposing boundary conditions provided by Baker Hughes and come from aerodynamic models data-matched on experimental test. Radial profiles of flow angles (blade-to-blade and meridional angles), total pressure and temperature are imposed at inlet section, relative to the TCF inlet, while the static pressure radial distribution is imposed at the outlet boundary, the TRF exit. Circumferential periodicity boundary conditions are applied to simulate the blade row channel alone with mixing plane approach. The CFD computations have been performed using the two-equation $\kappa - \omega$ turbulence model in the high Reynolds fully turbulent formulation. A maximum number of iterations or the residual value check is chosen to ensure a good numerical convergence. Then, the results are automatically post-processed in order to exchange the appropriate information with solid domain for static stress analysis.

4.3.2 Unsteady multi-row analysis

The aim of the unsteady multi-row analysis is to evaluate the harmonic content of the unsteady pressure distribution on the rotor blade (B3), due to the interactions with the upstream and downstream blade rows, necessary to perform the forced response analysis by means of the modal work calculation. The axial fluid domain is the same for the steady computations which includes the TCF and the TRF blade rows. So, the same H-type grid used for steady state calculations has been adopted. A full annulus approach with a total of 224 grid blocks with about 75 million of cells for inviscid endwall formulation, shown in Figure 4.7, and 235 million of cells for viscous approach, re-

spectively, has been used since the blades count from two adjacent rows has no a common divisor so it was not possible to reduce the computational domain to an angular sector.
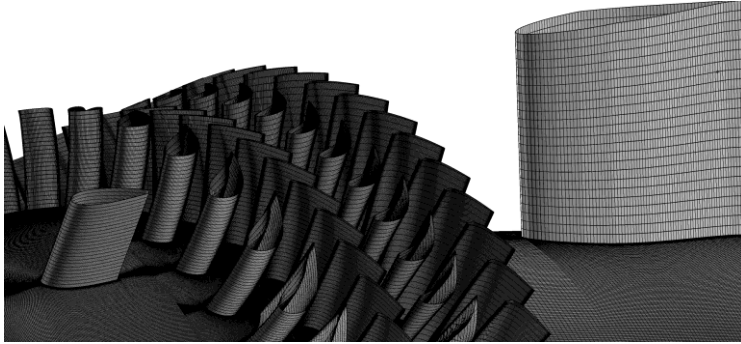
Figure 4.7: Full annulus computational mesh

This means that the entire wheel must be simulated leading to a higher computational cost. The computing resources, in terms of CPUs and computational time, has been provided by the Baker Hughes company on their cluster. The full annulus model adopts standard periodic boundary conditions with sliding interfaces between adjacent rows and buffer zones at the domain extremities to avoid spurious reflections [61]. To reach the flow periodicity, 5 rotor revolution periods have been necessary. The time discretization of the unsteady computations has been imposed adopting 50 time divisions for each blade passage of the row with the highest blade count in order to accurately solve the first 3 harmonics of the highest blade passing frequency related to the stator potential field disturbance. Each physical time step is converged with up to 15 sub-iterations. Both the operating conditions investigated through the unsteady analyses, design and off-design, have required 5 periods to reach periodicity starting from a steady state solution initialization. The

periodicity is considered to have been reached once the difference between the harmonics of the unsteady lift between two consecutive periods is less than a fixed tolerance. So, the unsteady calculations required about 2 or 6 days for the inviscid endwall and for the Full Navier-Stokes formulation, respectively using a parallel process involving 448 Intel® Xeon® Silver 4114 CPUs@2.20 GHz.

Once the solution periodicity is obtained, a run-time DFT can be activated during the last period of the URANS computations to extract the time Fourier coefficients of the solution on the selected blocks within the domain. Such coefficients are then extracted on the blade surface and split up into rotating perturbation with a dedicated post-processing tool.

4.4   Mode shapes transfer

As explained above, modal and structural analyses are not included in the present work and all the results come from a previous analysis carried out by Baker Hughes. The steps to obtain mode shapes and natural frequencies, already illustrated in Figure 4.1, are explained, focusing on the following phase in which the fluid and solid domain interact each other.

Starting from the FEM model, the solid domain is discretized to obtain a structured or unstructured grid as for the CFD model. Then, a modal analysis of a bladed disk sector in cyclic symmetry have been carried out by means of the FEM ANSYS solver. Natural frequencies and mode shape families are used to perform aerodynamic damping analysis and forced response assessments. In Figure 4.8 the normalized frequencies of the first three mode shapes families for rotor B3 are presented.
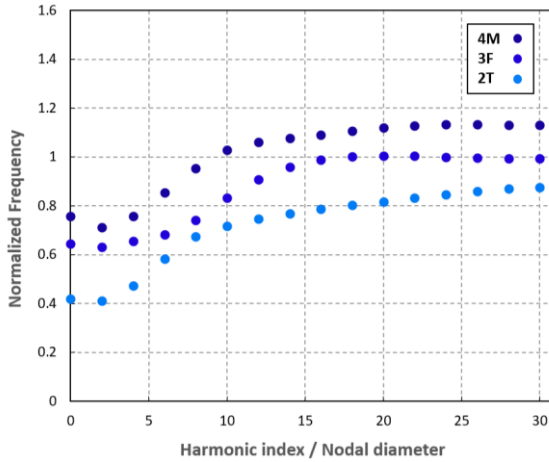
Figure 4.8: Mode shapes frequencies for rotor B3

Since the numerical method for aerodynamic damping computation is uncoupled, it is necessary to transfer mode shapes vibrations from the FEM surface elements to CFD blade surface, with the purpose of deforming fluid mesh during unsteady flutter computation with a defined amplitude. A dedicated tool performing an automatic roto-translation of the FEM blade shell to the CFD profile surface has been used. In Figure 4.9 the point clouds extracted from the two grids domains are shown (the FEM in green and the CFD in blue), respectively.
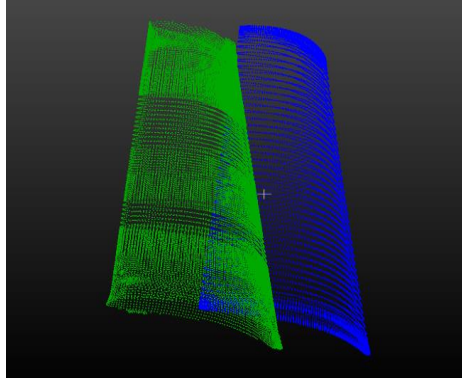
Figure 4.9: Point clouds of the FEM (green) and CFD (blue) blade surface grids

The interpolation of real or complex mode shapes displacements is also necessary as the CFD and FEM models have different discretization on the aerodynamic surfaces. Once the blade surface vibration has been transferred to the fluid mesh, an overall grid deformation strategy of the channel between blades based on an algebraic method is employed to make the row oscillate at the different traveling waves. This technique distributes the largest deformations where the biggest mesh elements are, while maintaining low deformations of the smallest elements to avoid cells intertwining during the entire blade vibration period. For complex mode shapes two homologous control nodes, which belong on the surfaces where the cyclic symmetry condition is applied, have to be considered in order to determine the travelling wave direction of the modal solution. Considering one of these nodes, a phase-shift related to the IBPA of a FTW and BTW is applied once each and compared with the second point displacements. The actual travelling wave direction is the one which provides minimum error obtained from the difference

between the IBPA phase shifting and the FTW or BTW. The overall blade row deformation, for all the possible travelling waves, may be then reproduced to each blade by rotating the mode shapes around the machine axis and, at the same time, by shifting the mode of the inter-blade phase angle. Opposite direction of travelling waves can be obtained by changing the IBPA sign and taking the complex conjugate of the mode shape displacements. The mode shape transfer results for a complex mode shape are reported in Figure 4.10.

Solid domain   Fluid domain
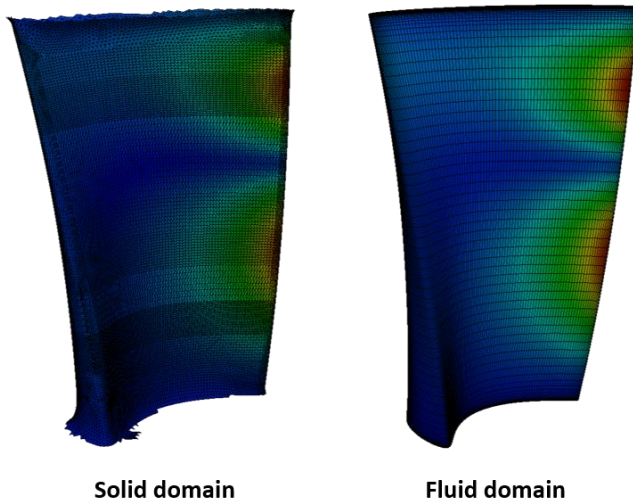
Figure 4.10: Example of the mode transfer from solid to fluid domain

4.5   Flutter analysis

Flutter evaluation is only performed on the rotor row where the risk of flutter occurrence is significantly higher. For this reason,

classical flutter computations consider an isolated row to which the vibration of the blade is applied as the only source of unsteadiness. Steady state and modal analysis results are used as input data for the unsteady flutter analysis and once mode shapes are transferred from solid to fluid domain the analysis can be performed with TRAF code. The aeroelastic solver employed an uncoupled method with a dual time stepping techniques, as already stated in paragraph 3.2.1. The number of subdivisions and the number of physical instants considered within an oscillation period need to be properly selected by the designer in order to choose the minimum values to ensure accurate solutions in terms of aerodynamic work and critical damping ratio. In this case, 15 periods of blade oscillations with a standard value of 80 equally spaced time steps for a single vibration have been computed. The solver is able to integrate the Navier-Stokes equations within a cell-centered finite volume fluid domain, whose boundaries move in accordance with the frequencies and mode shapes displacements obtained from modal analysis and to evaluate the unsteady pressure response over the blade surface while the blade row vibrates in a travelling wave manner when the computation reaches periodicity. The unsteady pressure is finally integrated during an oscillation period over the blade to obtain the aerodynamic damping parameters. Flutter stability is assessed by checking the sign of the aerodynamic work (Eq. (2.50)) done by the fluid onto the blade during one vibration period. A negative sign indicates a stable condition in which blade dissipates energy to the fluid, vice versa a positive sign denotes an unstable condition with the extraction of energy from the fluid to the blade. The critical damping ratio parameter may be also used for flutter stability evaluation, as explained in paragraph 4.5. From this parameter, it is possible to introduce a quantity, called energetic damping

coefficient surface density, which is a density of the energetic damping, defined as

$$\rho_\xi = \frac{-dW_{aero}}{8\pi E_{kin}\dfrac{d\Sigma}{\Sigma}} \qquad (4.1)$$

By integrating this local quantity over the whole blade surface the critical damping ratio can be obtained again. This parameter can be plotted over the blade surface, highlighting the areas of the blade that have more influence on global flutter stability.

4.6 Modal work calculation

The final outcome of a forced response analysis is the vibration response in terms of vibratory stress with respect to the allowable vibratory stress at the critical location of the blade. A scaling factor for the modal stress, coming from the modal analysis, is calculated by the tool to obtain the physical alternating stresses. Then, by means of a Goodman diagram, it is possible to assess the fatigue margin of the blade in a particular resonance condition.

The vibratory response of the blade can be determined when both the unsteady pressure distribution and the modal displacements are known for a given operating condition and a given frequency and nodal diameter. At this point, the forced response is computed by means of the modal work tool which takes as inputs the blade mode shape, the decomposed forcing functions, and the total damping. As for flutter analysis, blade mode shape is transferred on the CFD blade surface discretization: the choice of CFD discretization ensures a more accurate computation of the modal force. While the forcing functions have been

decomposed using the DFT, applied both in time and in space, the total damping value may come from numerical calculations, but it is preferable to leverage legacy data available from experimental tests of similar blades in comparable operating conditions. Total damping is inversely proportional to the amplification factor according to the usual definition used in literature:

$$Q = \frac{1}{2\delta_{tot}} \qquad (4.2)$$

For this study, a value of $Q = 100$ is given from experimental campaign as input data to obtain the total damping value.

The calculation of the modal force (or the modal work) reported in Eq. (2.46), allows to obtain the scaling factor value d, through which it is possible to scale down the modal stress to the actual vibratory stress during a resonance crossing.

5 Numerical results

In the first part of this chapter the steady state flow field results are presented. Steady results are compared with experimental data for the different formulations used in the CFD setup in order to highlight the best strategy for the following unsteady analyses. Then, unsteady analysis results are discussed both from an aerodynamic and an aeromechanic point of view. The aerodynamic flow field of the two operating conditions, design and off-design, is shown and compared. On the other hand, the frequency spectrum of the rotor blade load under investigation is analyzed, focusing on the blade-to-blade variability phenomenon. The effects of different numerical approaches and the variation between the two operating conditions are assessed. The forced response results obtained by the modal work computation are presented and compared with the measured data showing a good agreement. Finally, the unsteady flutter stability is assessed as well.

5.1 Steady state results: design point

The working condition where the aeromechanical assessment of the blade is required, is the design point, where the turbine commonly operates. Multi-row steady solution is useful both to initialize the unsteady computation, and to extract the boundary conditions on rotor row for a single row for flutter classical calculation. From steady state computation, the main aerodynamic data are extracted, in particular spanwise distributions of flow quantities (p_t, T_t) and isentropic Mach distributions at different blade span.

Steady CFD results are compared with the experimental data and the unsteady results in terms of spanwise distributions of total pressure and total temperature at STA 2.96, STA 5.00, and STA 3.00, as reported in Figure 5.1.

STA 2.96
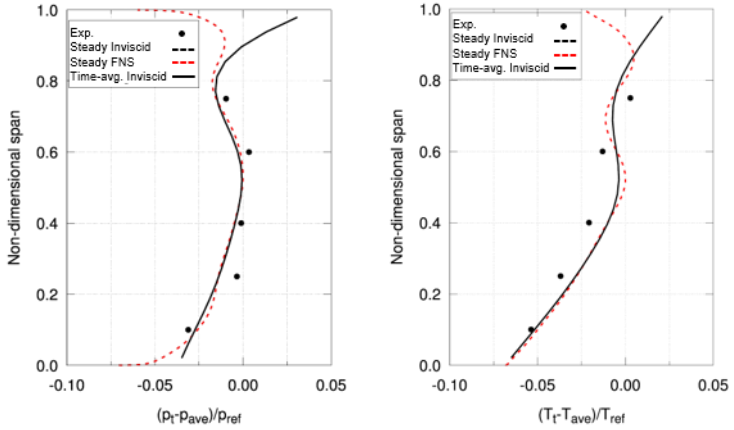
STA 3.00
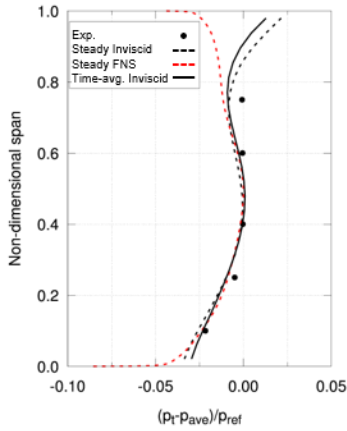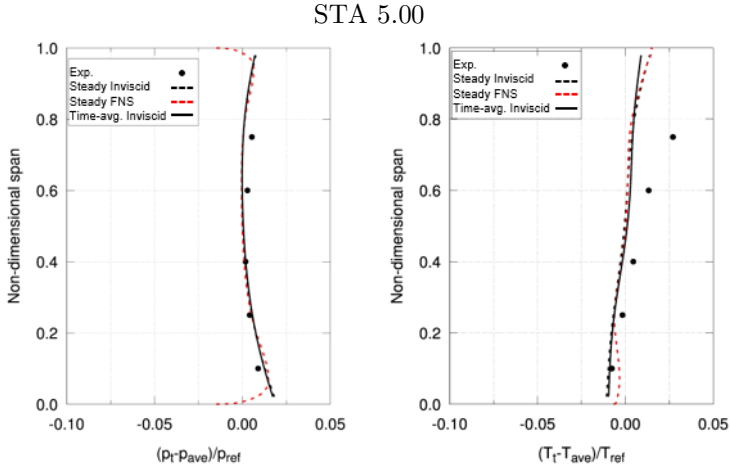
Figure 5.1: Total pressure and total temperature spanwise distributions: experimental, CFD steady with viscous and inviscid endwall formulation, and CFD time-averaged with inviscid formulation

An overall good agreement with experiments is observed in all the measurements stations. Some differences are pointed out at the leading edge of the TRF (STA5.00) near the outer diameter. In particular, the total temperature predicted by CFD is lower than the one measured, resulting in the over prediction of the LPT isentropic efficiency. In all the cross sections where measurements are available, both the results of the inviscid endwall formulation and the viscous Full Navier-Stokes approach are compared. As can be expected, even if the inviscid endwall approach cannot account for the development and transport of secondary flows, the two simulations show similar trends in the core flow region, while the differences are restricted to the regions close to the hub and shroud endwalls.

Furthermore, Figure 5.2 shows the time-averaged isentropic Mach number distributions for the rotor blade of Stage 3 (B3) at hub, midspan, and tip.
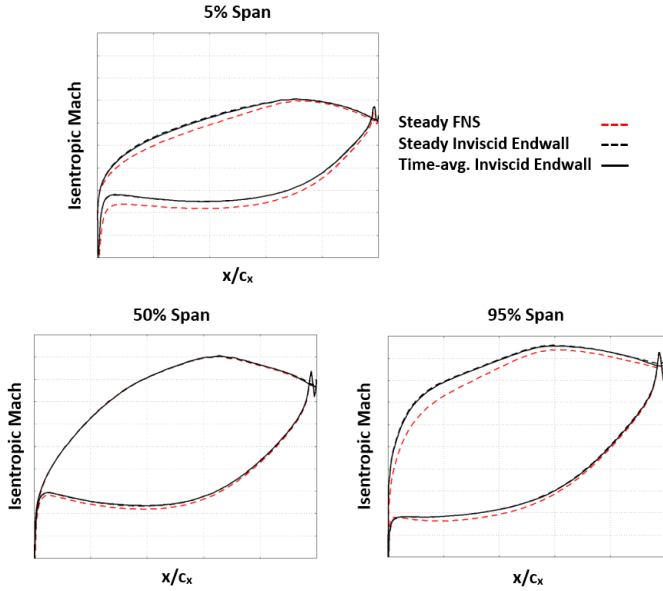
Figure 5.2: Isentropic Mach distributions at hub, midspan, and tip of blade: steady and time averaged results.

In the same figure a comparison is provided between the Full Navier-Stokes and the inviscid endwall approaches both in steady state simulation. Generally, the distributions are quite similar. Inviscid endwall and Full Navier-Stokes results show a good agreement except for the tip region (95% span), where some small discrepancies are observed in the peak Mach value. Similar considerations hold comparing steady and time-averaged results. In particular, at midspan, the comparison suggests that the inviscid endwalls calculations show good agreement with the Full Navier-Stokes. In light of such considerations, even

if the inviscid endwall approach does not account for the end-walls boundary layers and the related secondary flows, this strategy can be selected to carry out the unsteady calculation dedicated to the aeromechanical analysis in order to considerably reduce the whole computational effort.

In this work, unsteady analysis has been performed with both Full Navier-Stokes and inviscid endwall formulations, in order to compare the harmonics amplitudes extracted from the unsteady pressure distribution.

5.2   Unsteady results: design and off-design

Nowadays, the ability to simulate the entire domain of an axial gas turbine is an open challenge for many companies, both in terms of calculation resources and time. In this context, unsteady analyses can give useful feedbacks on the reliability of steady state simulations, which are used as a standard for routine design procedures. Unsteady results have been obtained for both formulations, Full Navier-Stokes and inviscid endwall. As shown in the former paragraph, the comparison with steady calculations and experimental data shows a good agreement. Furthermore, the two operating conditions, design (OP1) and off-design (OP2), have been investigated. Figure 5.3 illustrates a comparison of the instantaneous entropy field at midspan for the two operating conditions analyzed for inviscid endwalls formulation. With respect to the design condition, at partial load wider wakes, that are mixed downstream, are generated by the incidence variation on the TCF. These wakes persist through the four power turbine rows and leave a strong distortion pattern in the TRF region.
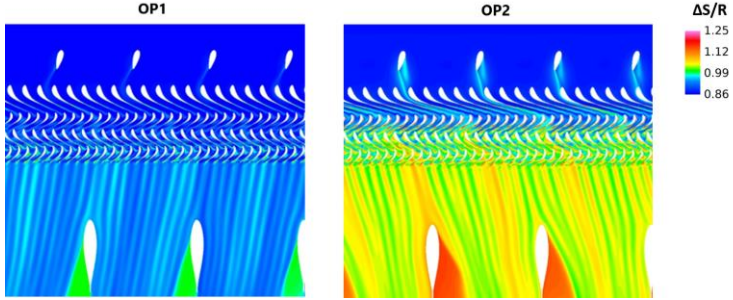
Figure 5.3: Instantaneous entropy contours of the two operative conditions at midspan. Design (left) and off-design (right) [**62**]

Concerning an aeromechanical point of view, the unsteady analysis focus on the extraction of the aerodynamic forcing functions and the study of the pressure harmonics content on the blade row. The analysis of the whole axial turbine domain allows the evaluation of the complete unsteady aerodynamic field and all the possible excitations generated by the multi-stage blade rows. Once the unsteady pressure time-history distribution over the blade surface is obtained by performing the post-processing of the solution with a run-time DFT in time, the frequency spectrum on the blade row surface is obtained. The unsteady lift amplitude is plotted as a function of the engine orders. For some peaks, this plot can show multiple points for each profile at a single engine order which indicates a blade-to-blade variability in terms of unsteady lift amplitude. An example of this phenomenon is reported in Figure 5.4 which shows the frequency spectrum of the unsteady blade loading of a low pressure turbine.
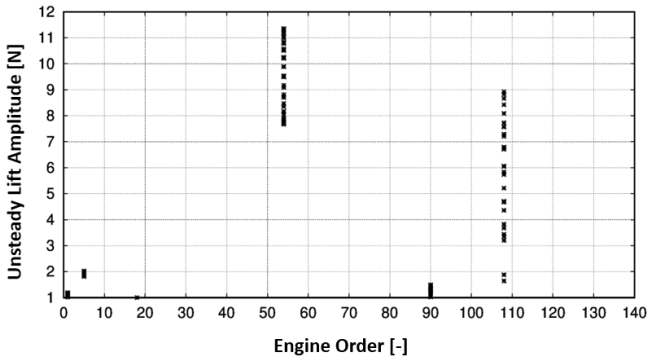
Figure 5.4: Example of frequency spectrum of unsteady blade loading

Each point corresponds to the unsteady lift amplitude value of a single airfoil constituting the blade row. All the engine orders that characterize the frequency spectrum show a relevant blade-to-blade variability in terms of unsteady lift amplitude due to the superpositions of two or more rotating unsteady pressure waves that share the same frequency, but different circumferential patterns. The superposition of these unsteady pressure waves occurs between blade rows in the same reference system, fixed or rotating.

In this work, the forcing functions effect on the Stage 3 rotor blade (B3) is evaluated. In Figure 5.5 the same plot representing the frequency spectrum for the blade row for the Full-Navier Stokes approach is shown.
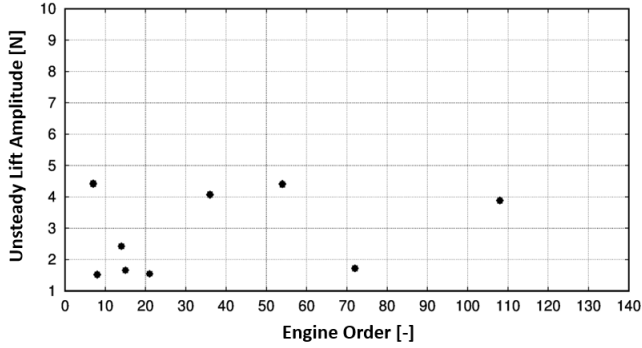
Figure 5.5: Rotor B3 frequency spectrum of unsteady blade loading

In this case, the variability is smaller since the considered row
is the first rotor and there are no further rotors upstream that
can generate additional rotating unsteady pressure waves. The
frequencies shown in Figure 5.5 correspond to the blade passing
frequencies (BPF) due to the upstream and downstream stator
rows. Considering that the analyzed domain is composed of the
rows listed in Table 5.1, where V3 and V4 indicate the stator
rows which have *N1* and *N2* blades number, respectively. On
the other hand, B3 and B4 are the rotor rows which have *N3*
and (*N2+2*) blade numbers. The rotor B3 is excited by the blade
passing frequency of the incoming wakes (BPF_{N1}) and the pas-
sage of downstream potential field (BPF_{N3}).

	V3	**B3**	**V4**	**B4**
Blade number	N1	N2	N3	N2+2

Table 5.1: Blade number of each row

It must be also pointed out that multiple frequency (related to harmonic index greater than 1) are clearly visible in the spectrum which are *2BPF$_{N1}$*, *2BPF$_{N3}$*, and *BPF$_{N3}$-BPF$_{N2}$* with a lower intensity. Since the crossing occurs for the *BPF$_{N1}$*, an in-depth analysis is requested to evaluate if the vibration limits imposed by the specifications are respected.

The unsteady forcing of the rotor B3 due to the engine order excitation of stator V3 has been investigated. Figure 5.6 shows the blade-to-blade variation of unsteady lift amplitude of the *BPF$_{N1}$* on B3.
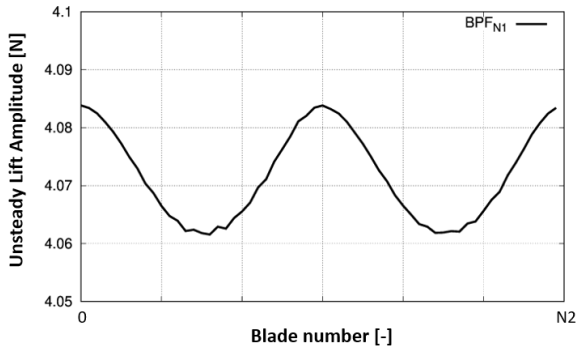
Figure 5.6: Unsteady lift amplitude of *BPF$_{N1}$* on B3

The plot shows the circumferential variation of the unsteady lift amplitude due to the interaction of rotor rows with stator rows. To confirm the lower variability, note the narrow scale on the y-axis. The sinusoidal pattern has two peaks linked to the difference between the blade count of B3 and B4:

$$B3 - B4 = N2 - (N2 + 2) = 2 \tag{5.1}$$

The variation of the unsteady lift amplitude on B3 row confirms that the tangential distortions are due to blade row in the same frame of reference with a different count.

Applying the circumferential DFT to the unsteady pressure time Fourier complex coefficients on the blade surface, the contribution of the different nodal diameters can be finally separated.

Figure 5.7 shows the maximum value of the amplitude of the time-space Fourier coefficients of the BPF_{N1} on B3 blade surface decomposed into all the possible circumferential order m that will excite the corresponding NDs.
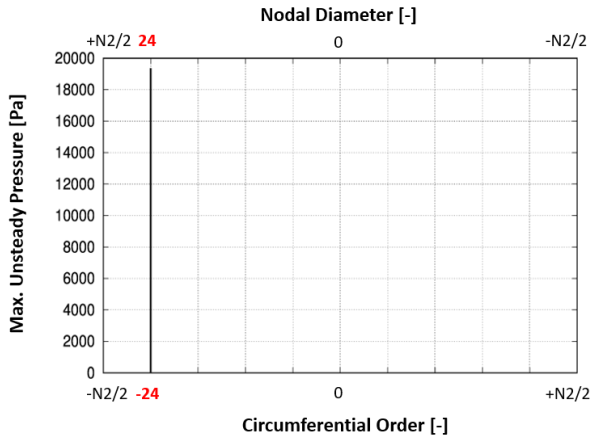
Figure 5.7: Maximum unsteady pressure amplitude of BPF_{N1} of B3 blade surface vs. circumferential order and nodal diameter

The unsteady forces of the BPF_{N1} are generated by the circumferential order m obtained by the main interaction with V3 and B3 (in the different frame of reference of the rotor),

$$m = N1 - N2 = -24 \rightarrow ND = 24 \qquad (5.2)$$

that correspond to a positive nodal diameter. The sign on the
ND is referred to the rotational direction of the spinning pertur-
bation compared with the rotational speed direction, and it is
negative if the spinning perturbation runs forward respect to
B3, whereas it is positive if the forcing runs backward respect
to B3. Then, checking in the interference diagram of rotor B3,
the Zig-Zag line corresponding to the OP1 corrected speed (Ta-
ble 4.1) intersects the frequency of the mode shape family inves-
tigated in the nodal diameter *ND*=24 as shown in Figure 5.8.
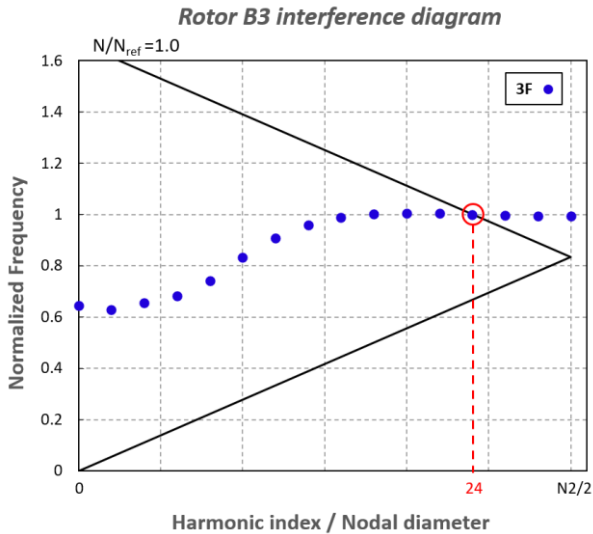
Figure 5.8: B3 interference diagram OP1 condition

5.2.1 Numerical approach comparison

Unsteady simulations have been performed with both viscous
Full Navier-Stokes and inviscid endwall setups. This has allowed
to evaluate the effects that these two different approaches have
on the extraction of the aerodynamic forcing functions and on

blade lift amplitude. Firstly, the comparison of the frequency spectrum seen by rotor B3 for both cases is shown in Figure 5.9.
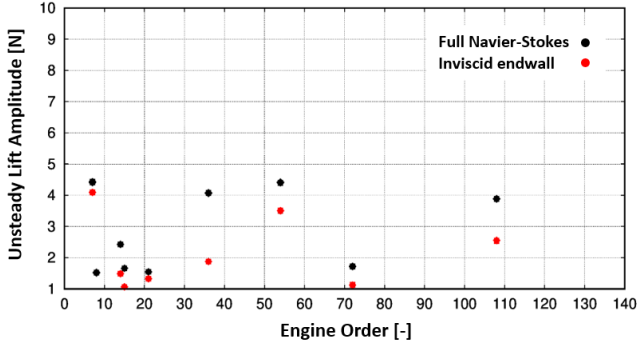
Figure 5.9: B3 spectrum frequency: Full Navier-Stokes vs inviscid endwall formulation

Looking at the plot, some differences between two analyses are visible given that the inviscid endwall formulation has no grid refinement in the endwall regions leading to a minor blockage. To support this, the isentropic Mach distributions for three different blade spans have been reported in Figure 5.10. The only differences are at the hub and tip sections, 5% and 95% of the span respectively, where the two curves slightly diverge considering that inviscid endwall formulation cannot account for the development and transport of secondary flows.
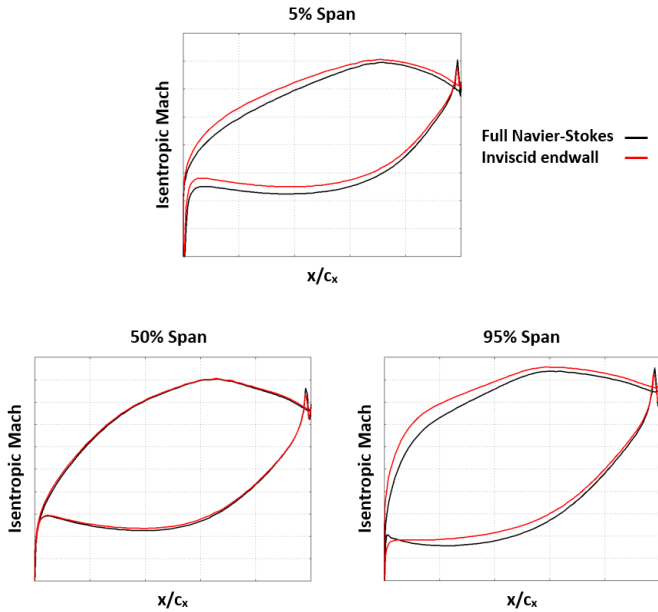
Figure 5.10: Comparison of isentropic Mach distribution at 5%, 50% and 95% span

Then, considering the result of the circumferential decomposition, the difference is also visible in the blade-to-blade variation of the unsteady lift amplitude (Figure 5.11). The Full Navier-Stokes formulation shows higher values due to the secondary flow effects, but the sinusoidal trend is always observed.
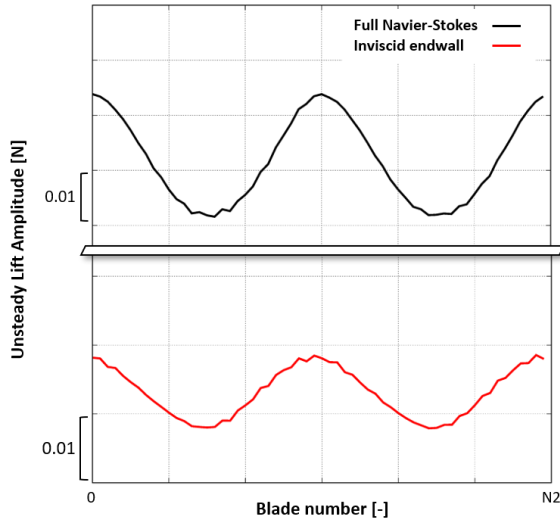
Figure 5.11: Unsteady lift amplitude: Full Navier-Stokes vs inviscid endwall formulation

5.2.2 Operative point change effects: inviscid endwall

Once the two numerical approaches have been compared, the results for the two operating conditions investigated, design and off-design, have been analyzed with the inviscid endwall approach. Some difference can be observed as well. In off-design condition, the harmonic content of some frequencies decreases or even disappear, while other frequencies are more present, revealing a greater contribution than the design condition, as shown by Figure 5.12.
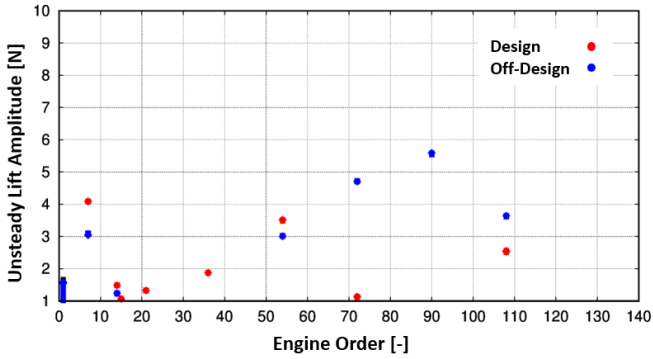
Figure 5.12: B3 spectrum frequency: design vs off-design condition

When analysing the unsteady lift amplitude on the rotor B3, the tangential distortion, due to the different blade count between blade rows in the same frame of reference, occurs but with widely different values (Figure 5.13). This difference is due to the re-stagger of the NGV profile that reduces the vane throat area at off-design condition. Consequently, the LPT rotor (B3) works with high incidence angle with respect to the design condition. This leads to the onset of a small flow separation near the leading edge that is transported downstream during the rotor motion and which impacts on the harmonic content (Figure 5.12).
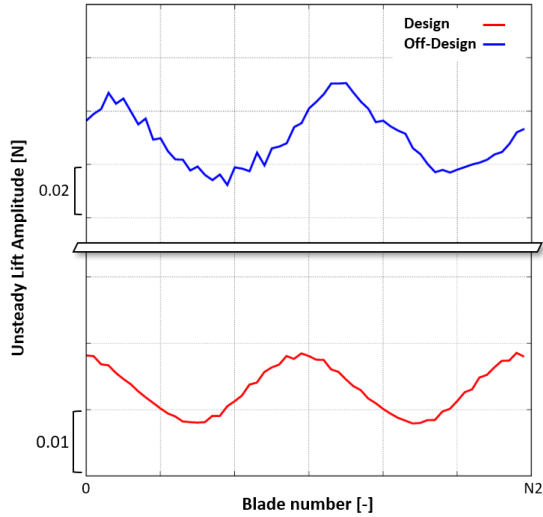
Figure 5.13: Unsteady lift amplitude: design vs off-design condition

This higher difference in the unsteady lift amplitude value for the two operating conditions is justified by the different load to which the blade itself is subject, as seen from the isentropic Mach distribution shown in the Figure 5.14.
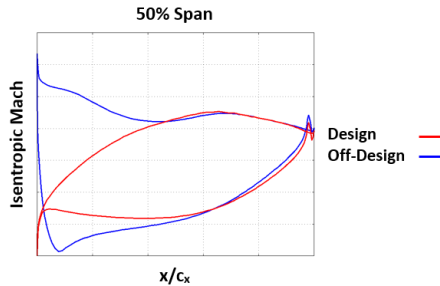
Figure 5.14: Comparison of isentropic Mach distribution at 50% span

5.3   Modal work results

The unsteady CFD analysis of the complete turbine domain has been performed to obtain the unsteady pressure fluctuation of rotor blade B3. Then, the spatial decomposition process has been applied to extract the unsteady pressure component that excites the *ND*=24, rotating in the forward direction. On the other hand, from the modal analysis, the modal displacements have been calculated for this nodal diameter. Finally, the last input for the forced response analysis is the total damping, that has been calculated starting from the amplification factor *Q.* In this work, the damping value is obtained applying a *Q* factor of 100 coming from the experimental campaign. Entering all these inputs into the modal work tool, the scaling factor is calculated and applied to modal displacement and stresses.
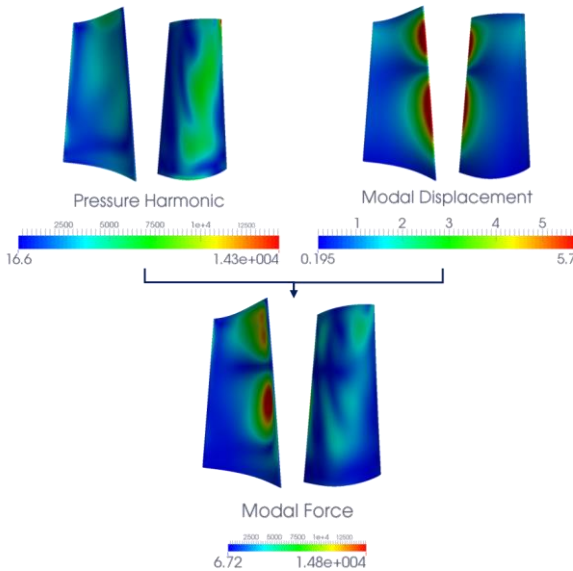
Figure 5.15: Pressure harmonic, modal displacements, and modal force blade contours

Table 5.2 summarized the main inputs and the final output for the forced response calculation by modal work approach. The comparison between the measured and calculated results obtained shows a good agreement. The predicted response value falls between the experimental data range. The response of rotor blade B3 is safely below the response limit imposed.

ND	Normalized Frequency [-]	Measured Q factor [-]	Measured Response [$\mu\varepsilon$]	Predicted Response [$\mu\varepsilon$]
24	1.00	100	55-60	57.5

Table 5.2: S3B rotor response

5.4   Flutter results

Lastly, the flutter stability assessment has been performed for all the fourth mode shape family (which include the *ND*=24 mode shape previously analyzed) of rotor blade B3, as shown in Figure 5.8. The unsteady CFD flutter analysis has been carried out for all the even nodal diameters in order to reduce the computational cost but, at the same time, to ensure a good discretization of the aerodynamic damping curve. Flutter results are shown in Figure 5.16 where the critical damping ratio ξ curve is reported for the selected nodal diameters. Flutter stability can be detected for all nodal diameters range since all nodal diameters show positive critical damping ratio values. The curve also highlights a quasi-symmetrical trend with respect to the *ND*=0.
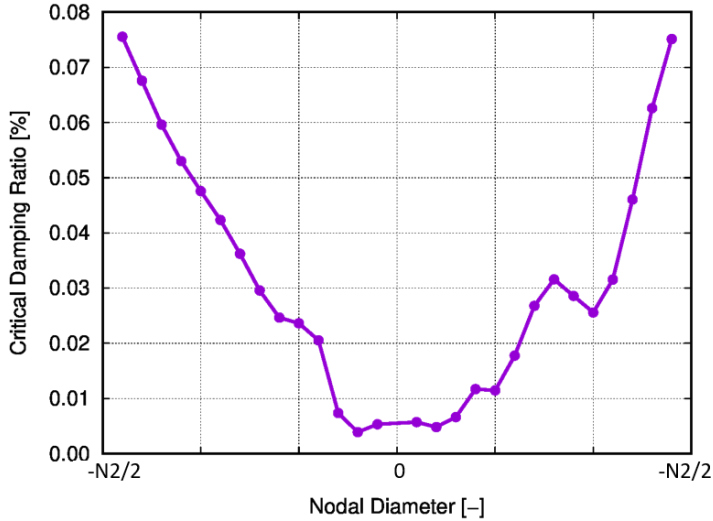
Figure 5.16: Critical damping ratio curve

Flutter analysis allows the computation of the aerodynamic damping values for each nodal diameter considered. As expected, a considerably lower value compared to the total damping one is obtained since for these blades the structural damping value is recognized to be higher than the aerodynamic one because of the presence of damping devices.

For the investigated nodal diameter, the ND=24, the energetic damping coefficient surface density, defined in Eq. (4.1, is plotted on the blade surface on pressure and suction side (Figure 5.17). This quantity highlights where stable and unstable areas locally arise on the blade surfaces. Blue zones identify regions where the blade oscillation is locally damped by unsteady flow, while red zones individuate the regions where fluid flow is feeding energy to the blade. The wide blue area confirms the stability condition for the rotor blade B3 at the ND=24.
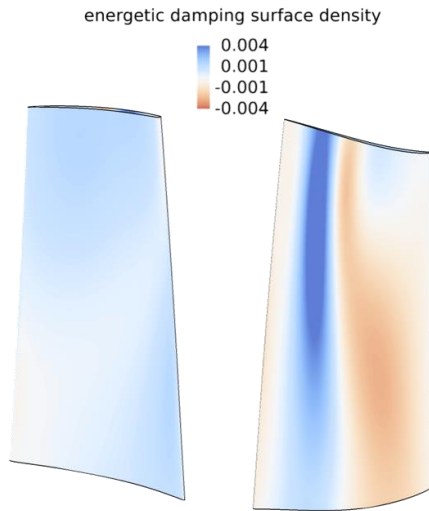
Figure 5.17: Energetic damping coefficient surface density for
ND=24

6 Conclusions

The development and the application of an integrated procedure for the aerodynamic and the aeromechanic design of axial gas turbine engines has been presented in this thesis. The purpose of this work is to analyze by means of numerical simulations the aerodynamic and aeromechanic design of a multi-stage axial turbine in order to prevent and avoid any vibration issues due to forced response and flutter phenomena. Considering the current state-of-the-art, such an achievement could lead to a significant saving of time in the design chain iterations and to better and safer performing machines.

This strategy begins considering the aerodynamic design phase necessary to evaluate the overall performance of axial gas turbines. The study of the main design parameters of a turbine stage allow the definition of the flow function and the efficiency curves for both a single and the all turbine stages. In this context, axial turbine maps are the final outcome of the preliminary design, used to select the best solution. A re-interpretation of these characteristics curves has been presented in order to provide a clearer and more intuitive use. Steady and unsteady CFD analyses are then performed to study the flow field structures and the main rotor/stator interactions. On the other hand, the aeromechanical design is carried out to predict forced response or flutter onset on turbomachinery components to eliminate HCF failures in the design phase. From FEM modal analyses, natural frequencies and mode shapes families of the blade row under investigation are obtained. The designer can use usual tools, like Campbell or ZZENF diagrams, to predict if resonances are present. The last step is the forced response analysis,

with the blade row HCF life evaluation by means of the Goodman's diagram. These two sides of the overall design, aerodynamic and aeromechanical, are combined with the use of numerical simulations. In fact, unsteady CFD analyses allow a detailed study of the aerodynamic phenomena of a multi-row turbine and, at the same time, allows the extraction of the aerodynamic forcing functions necessary as input in a forced response analysis. Furthermore, the modal force and flutter calculations are performed once the mode shapes displacements are transferred from solid to fluid domain.

The activity has been carried out in the framework of the collaboration between the university research group led by Professor Arnone and the industrial partner Baker Hughes. This procedure has been applied on a heavy-duty LP turbine of the Baker Hughes family. Forced response calculation and flutter stability assessment have been performed on the rotor of the first stage (Stage 3) and the results, coming from the CFD simulations, have been compared with experimental measurements. CFD analyses are the focus of this work, while the modal and structural analyses come from a previous activity by Baker Hughes. All the numerical simulations have been performed with the in-house developed CFD code TRAF. Two different operating points have been investigated, the design and an off-design condition. Starting from the discretization of the computational fluid domain, steady-state analyses have been carried out to closely match the experimental data and to initialize the unsteady analysis. Two different numerical approaches have been adopted, the inviscid endwall and the full-Navier Stokes formulation. The first one allows, where applicable, to considerably reduce the computational cost of CFD analyses without losing the solution accuracy. Then, the full annulus unsteady analyses have been performed and post-processed applying a

DFT in time. Analyzing the frequency spectrum, which shows all the *BPFs* that excite the blade row, a blade-to-blade variability of the unsteady lift amplitude has been observed for different engine orders. This phenomenon is caused by the superpositions of two or more rotating unsteady pressure waves that share the same frequency, but with different circumferential patterns. Furthermore, looking at the unsteady lift amplitude distribution for the investigated *BPF* on rotor blade, a further variation with a sinusoidal trend has been observed. This can be justified by the combination of spinning harmonics belonging to blade rows with different count in the same frame of reference. Finally, applying the DFT in space, the contribution of the different nodal diameters has been decomposed and the effect of the single nodal diameter can be evaluated. The analyses have demonstrated that the spatial content associated to the different time harmonics may be originated by Tyler-Sofrin acoustic interactions, usually considered in aeroacoustics analysis only. The proposed approach allows to identify all the possible additional excitation sources present in a multi-row environment with respect to the traditional stator-rotor unsteady analysis that considers only the contribution of the main interactions. Similar conclusions have been obtained by comparing the results of the analysis with the two different numerical approaches and for the two different operative conditions.

Finally, the forced response has been computed by means of the modal work approach which combines the blade mode shape displacements with the decomposed forcing functions, and the total damping. This latter input has been calculated from the amplification factor value provided by measured data. The predicted response value in terms of vibration stresses is in good agreement with the experimental data and the response of rotor is safely below the response limit imposed. A further result of

this work is the flutter stability assessment. The unsteady CFD flutter results, obtained using an uncoupled non-linear method, show positive critical damping ratio values for all nodal diameters range, underlining a stable behavior for the investigated family. Moreover, this analysis confirms that the aerodynamic damping values are lower compared with the total damping acquired during the experimental campaign. This seems to be consistent, since structural damping value is much higher for this type of blade rows which include many types of dampers.

Possible future works may involve the optimization of the integrated procedure process, making it faster in order to further reduce computational time. This could open the possibility to be widely adopted in the industrial field to perform unsteady analyses of entire turbine domains faster and to obtain an aeromechanical design and a forced response assessment in a more reliable way. A further aspect to be included is the study of the impact of the cooling flows on the harmonic content, considering the high pressure turbine module. Source terms coming from cooling may modify the internal flow field, and this could lead to a variation of the amplitude of the forcing functions.

References

[1]   J. Dahl, «Jet engine - Wikipedia, the free encyclopedia,» 2007.   [Online].   Available: https://en.wikipedia.org/wiki/Jet_engine#/media/File:J et_engine.svg.

[2]   H. Cohen, G. F. C. Rogers e H. I. H. Saravanamuttoo, Gas Turbine Theory, Longman Group, 1996.

[3]   T. Giampaolo, Gas Turbine Handbook:, Lilburn, GA: The Fairmont Press, Inc., 2006.

[4]   C. M. Soare, «Gas Turbines in Simple Cycle & Combined,» in *Gas Turbines: A Handbook of Land, Sea and Air Applications*, Butterworth Heinemann, BH.

[5]   M. P. Boyce, Gas Turbine Engineering Handbook - 2nd edition, Houston, Texas: Butterworth-Heinemann, 2002.

[6]   S. Lieblein, F. C. Schwenk e R. L. and Broderick, «Diffusion Factor for Estimating Losses and Limiting Blade Loadings in Axial Flow Compressor Blade Elements,» in *Technical report, National Advisory Committee for Aeronautics*, Cleveland, 1953.

[7]   S. F. Smith, «A Simple Correlation of Turbine Efficiency,» *Journal of Royal Aeronautical Society,* vol. 69, n. 7, pp. 467-470, 1965.

[8]   S. a. G. R. Havakechian, «Aerodynamic design of 50 percent reaction steam turbines,» *Proceedings of the Institution of Mechanical Engineers, Part C: Journal of*

Mechanical Engineering Science, , vol. 213, n. 1, pp. 1-25, 1999.

[9]   M. T. Schobeiri, Gas Turbine Design, Components and System Design Integration, Springer, 2018.

[10] J. D. Denton, "Loss Mechanisms in Turbomachines," *ASME Journal of Turbomachinery,* vol. 115, pp. 621-656, 1993.

[11] J. H. Horlock, Axial Flow Turbines, Melbourne, FL, USA: Kreiger Publishing Co., 1973.

[12] H. J. A. Craig e H. R. M. Cox, «Performance Estimation of Axial Flow Turbines,» *Proc. Instn. Mech. Engrs.,* vol. 185, pp. 407-424, 1970.

[13] S. a. O. U. Kacker, «A Mean Line Prediction Methods for Axial Flow Turbine Efficiency,» *J. of Engineering for Power,* vol. 104, n. 1, pp. 111-119, 1982.

[14] D. a. M. G. Ainley, «An Examination of the Flow and Pressure Losses in Blade Rows of Axial Flow Turbines,» *R.&M.,* vol. 2891, 1955.

[15] S. L. Dixon and C. A. Hall, Fluid Mechanics and Thermodynamics of Turbomachinery, Elsevier Inc., 2014.

[16] A. Scotti Del Greco, S. Biagiotti, V. Michelassi, T. Jurek, D. Di Benedetto, S. Francini e M. Marconcini, «Analysis of Measured and Predicted Turbine Maps From Start-Up to Design Point,» *ASME Turbo Expo 2020*

Turbomachinery Technical Conference and Exposition, 2020.

[17] P. S. Patil e S. L. Borse, «Recent Studies in Internal Cooling of gas turbine blade: a Review,» *International Journal of Applied Engineering Research,* vol. 13, n. 9, pp. 7131-7141, 2018.

[18] A. R. Collar, «The expanding domain of aeroelasticity,» *The Aeronautical Journal,* vol. 50, n. 428, pp. 613-636, 1946.

[19] Y. C. Fung, An introduction to the theory of aeroelasticity, Courier Dover Publications, 2008.

[20] D. Vogt, «FUTURE - Deliverable Report,» in *FUTURE report No: FTR-5-85*, 2013.

[21] M. P. Castanier e P. C., «Modeling and analysis of mistuned bladed disk vibration: current status and emerging directions,» *Journal of Propulsion and Power,,* vol. 22, n. 2, p. 384–396, 2006.

[22] J. K. Ramsey, NASA aeroelasticity handbook volume 2: design guides part 2, 2006.

[23] M. A. Mayorca, *Numerical Methods for Turbomachinery Aeromechanical,* 2011.

[24] S. J. Wildheim, «Excitation of rotationally periodic structures,» *Journal of Applied Mechanics,* vol. 46, n. 4, pp. 878-882, 1979.

[25] M. P. Singh, J. J. Vargo, D. M. Schiffer e J. D. Dello, «SAFE Diagram-A Design and Reliability Tool for Turbine Blading,» *Proceedings of the Turbomachinery Symposium* , vol. 17, pp. 93-101, 1988.

[26] L. Pinelli, C. Burberi, M. Ignesti, V. Michelassi, L. Tapinassi, A. Abati e R. Pacciani, «Spatial Decomposition of Aerodynamic Forcing and Interference Diagram - Part I: Theory and Aeromechanic Validation on an Industrial Axial Compressor,» *Proceedings of ASME Turbomachinery Technical Conference and Exposition,* n. Paper No. GT2021-59514, 2021.

[27] J. M. Tyler e T. G. Sofrin, «"Axial flow compressor noise studies",» *SAE Transactions,* vol. 70, pp. 309-332, 1962.

[28] T. Nicholas e J. R. Zuiker, «On the use of the Goodman diagram for high cycle fatigue design,» *International Journal of Fracture,* vol. 80, pp. 219-235, 1996.

[29] M. H. Herman Shen, «Reliability assessment of high cycle fatigue design of gas turbine blades using the probabilistic Goodman diagram,» *International Journal of fatigue,* vol. 21, n. 7, p. 699–708, 1999.

[30] H. Ferria, *Contribution to Numerical and Experimental Studies of Flutter in Space Turbines. Aerodynamic Analysis of Subsonic or Supersonic Flows in Response to a Prescribed Vibratory Mode of the Structure,* 2011.

[31] J. G. Marshall e M. Imregun, «A review of aeroelasticity methods with emphasis on turbomachinery applications,»

Journal of Fluids and Structures, vol. 10, pp. 237-267, 1996.

[32] A. V. Srinivasan, "Flutter and resonant vibration characteristics fo engine blade," *ASME International Gas Turbine and Aeroengine Congress and Exhibition,* vol. 119, no. 4, pp. 742-775, 1997.

[33] D. Vogt, *Experimental Investigation of Three-Dimensional Mechanisms in Low-Pressure Turbine Flutter,* 2005.

[34] A. Arnone, ""Viscous Analysis of Three–Dimensional Rotor Flow Using a Multigrid Method"," *J. Turbomach.,* vol. 116, no. 3, pp. 435-445, 1994.

[35] A. Arnone, M. S. Liou e L. A. Povinelli, «Multigrid calculation of three-dimensional viscous cascade flows,» *Journal of propulsion and power,* vol. 9, n. 4, pp. 605-614, 1993.

[36] B. S. Baldwin and H. Lomax, "Thin Layer Approximation and Algebraic Model for Separated Turbulent Flows," *AIAA paper 78-257,* 1978.

[37] D. Degani and L. B. Schiff, "Computation of Turbulent Supersonic Flows Around Pointed Bodies Having Crossflow Separation," *Journal of Computational Physics,* vol. 66, pp. 173-196, 1986.

[38] A. Arnone and R. Pacciani, "IGV-Rotor Interaction Analysis in a Transonic Compressor Using the Navier-

Stokes Equations," *ASME Journal of Turbomachinery,* vol. 120, pp. 143-155, 1 1998.

[39] P. R. Spalart and S. R. Allmaras, "A One-equation Turbulence Model for Aerodynamic Flows," *AIAA Paper 92-0439,* 1 1992.

[40] P. R. Spalart and M. Shur, ""On the Sensitization of Turbulence Models to Rotation and Curvature"," *Aerospace Science and Technology,* vol. 1, pp. 297-302, 1997.

[41] D. C. Wilcox, "Turbulence Modeling for CFD", 2nd ed., La Cañada, CA, USA: DCW Ind. Inc., 1998.

[42] D. C. Wilcox, "Formulation of the k-ω Turbulence Model Revisited," *AIAAJ,* vol. 46, pp. 2823-2838, 11 2008.

[43] F. R. Menter, "Two-Equations Eddy Viscosity Turbulence Models for Engineering Applications," *AIAA J.,* vol. 32, pp. 1598-1605, 8 1994.

[44] R. H. Ni, "A Multiple-Grid Scheme for Solving the Euler Equations," *AIAA paper 81-1025,* 1981.

[45] A. Jameson, W. Schmidt and E. Turkel, "Numerical Solutions of the Euler Equations by Finite Volume Methods Using Runge--Kutta Time--Stepping Schemes," *AIAA paper 81--1259,* 1981.

[46] R. C. Swanson and E. Turkel, ""On Central-Difference and Upwind Schemes"," *Journal of Computational Physics,* vol. 101, pp. 292-306, 1992.

[47] R. C. Swanson and E. Turkel, "Artificial Dissipation and Central Difference Schemes for the Euler and Navier-Stokes Equations," *AIAA paper 87--1107--CP,* 1987.

[48] P. L. Roe and M. J. Baines, "Algorithms for advection and shock problems," in *Proceedings of the Fourth GAMM Conference on Numerical Methods in Fluid Mechanics, Notes on Numerical Fluid Mechanics, 5; p. 281*, Vieweg, 1981.

[49] M. Arora and P. L. Roe, "A Well-Behaved TVD Limiter for High-Resolution Calculations of Unsteady Flow," *Journal of Computational Physics,* vol. 132, pp. 3-11, 1997.

[50] A. Arnone, "Multigrid Methods for Turbomachinery Navier-Stokes Calculations," in *Solution Techniques for Large-Scale CFD Problems*, 1995.

[51] M. Raw, «Robustness of coupled algebraic multigrid for the Navier-Stokes equations,» in *In 34th Aerospace sciences meeting and exhibit*, 1996.

[52] G. Wittum, «The use of fast solver in computational fluid dynamics,» *Proceedings of the Eighth GAMM-Conference on Numerical Methods in Fluid Mechanics,* p. pages 574–581, 1990.

[53] L. Cozzi, F. Rubechini, M. Marconcini, A. Arnone, P. Astrua, A. Schneider and A. Silingardi, "Facing the Challenges in CFD Modelling of Multistage Axial Compressors," in *Proceedings of ASME Turbo Expo 2017:*

Turbomachinery Technical Conference and Exposition, Charlotte, NC, USA, 2017.

[54] M. Giovannini, M. Marconcini, A. Arnone and A. Dominguez, "A Hybrid Parallelization Strategy of a CFD Code for Turbomachinery Applications," in *11th European Turbomachinery Conference, paper ETC2015-188*, Madrid, 2015.

[55] F. O. Carta, «Coupled blade-disk-shroud flutter instabilities in turbojet engine rotors,» *Journal of Engineering for Power,* vol. 89, n. 3, pp. 419-426, 1967.

[56] T. G. Keith, J. G. L. Stefko, R. Srivastava e M. A. Bakhle, «Aeroelastic analysis of turbomachinery: Part I - phase lagged boundary condition,» *International Journal of Numerical Methods for Heat & Fluid Flow,* vol. 14, n. 3, pp. 366-381, 2004.

[57] M. Giovannini, M. Marconcini, A. Arnone and F. Bertini, ""Evaluation of Unsteady Computational Fluid Dynamics Models Applied to the Analysis of a Transonic High-Pressure Turbine Stage"," *Part A: Journal of Power and Energy,* vol. 228, no. 7, p. 813–824, 2014.

[58] S. Moffatt e L. He, «Blade Forced Response Prediction for Industrial Gas Turbines: Part 1 — Methodologies,» *Proceedings of the ASME Turbo Expo 2003 - Power for Land, Sea, and Air,* vol. 4, pp. 407-414, 2003.

[59] W. Ning, S. Moffatt, Y. Li e R. Wells, «Blade forced response prediction for industrial gas turbines - Part 2: verification and application,» *Proceedings of ASME*

Turbo Expo 2003 - Power for Land, Sea and Air, vol. 4, pp. 415-422, 2003.

[60] F. Eichner e J. Belz, «Application of the modal approach for prediction of forced response amplitudes for fan blades,» *roceedings of the ASME Turbo Expo 2018: Turbomachinery Technical Conference and Exposition,* vol. 7C, 2018.

[61] P. Gaetani, G. Persico, L. Pinelli, M. Marconcini e R. Pacciani, «Computational and Experimental Study of Hot Streak Transport Within the First Stage of a Gas Turbine,» *ASME Journal of Turbomachinery,* vol. 142, n. 8, p. 081002, 2020.

[62] S. Biagiotti, J. Bellucci, M. Marconcini, A. Arnone, G. Baldi, M. Ignesti, V. Michelassi e L. Tapinassi, «Impact of Turbine Center Frame Wakes on Downstream Rows in Heavy Duty Low Pressure Turbine,» *ASME Journal of Turbomachinery,* vol. Volume 2A: Turbomachinery, pp. Paper No. GT2019-90721, 2019.

[63] F. Vanti, A. Agnolucci, L. Pinelli e A. Arnone, «An integrated numerical procedure for flutter and forced response assessment of turbomachinery blade-rows,» *Proceedings of 13th European Conference on Turbomachinery Fluid dynamics & Thermodynamics, ETC13,* n. Paper ID: ETC2019-199, 2019.